Impact of wildfire smoke on Arctic cirrus formation, part 1: analysis of MOSAiC 2019-2020 observations

Albert Ansmann[1], Cristofer Jimenez[1], Johanna Roschke[1], Johannes Bühl[1,2], Kevin Ohneiser[1], Ronny Engelmann[1], Martin Radenz[1], Hannes Griesche[1], Julian Hofer[1], Dietrich Althausen[1], Daniel A. Knopf[3], Sandro Dahlke[4], Tom Gaudek[1], Patric Seifert[1], and Ulla Wandinger[1]

[1]Leibniz Institute for Tropospheric Research, Leipzig, Germany
[2]Harz University of Applied Sciences, Wernigerode, Germany
[3]School of Marine and Atmospheric Sciences, Stony Brook University, Stony Brook, NY 11794, USA
[4]Alfred Wegener Institute, Helmholtz Centre for Polar and Marine Research, Potsdam, Germany

Correspondence: A. Ansmann
(albert@tropos.de)

Abstract.

The number of wildfire smoke layers in the upper troposphere per fire season increased at mid and high northern latitudes during the last years. To consider smoke in weather and climate models appropriately, the influence of smoke on a variety of atmospheric processes needs to be explored in detail. In this study, we focus on the potential impact of wildfire smoke on cirrus formation. For the first time, state-of-the-art aerosol and cirrus observations with lidar and radar, presented in part 1 of a series of two articles, are closely linked to comprehensive modeling of gravity-wave-induced ice nucleation in cirrus evolution processes, presented in part 2. The complex study is based on aerosol and ice cloud observations in the central Arctic during the one-year MOSAiC (Multidisciplinary drifting Observatory for the Study of Arctic Climate) expedition. For almost a year (from the summer of 2019 to the spring of 2020), aged Siberian wildfire smoke polluted the tropopause region over the central Arctic and many cirrus systems developed in the polluted upper troposphere. Goal of the data analysis (part 1) is to provide observational evidence for a dominating impact of aged wildfire smoke (organic aerosol particles) on cirrus formation in the central Arctic (over the MOSAiC research icebreaker Polarstern) during the winter half year of 2019-2020. Aim of the simulations in part 2 is to gain a deeper and more detailed insight into the potential smoke impact on ice nucleation as a function of observed aerosol and meteorological conditions (temperature, relative humidity) and by considering realistic gravity wave characteristics (updraft speed, wave amplitude). Vertical movements of air parcels are essential to initiate cloud formation. The measurements presented in part 1 were conducted during the winter half year (October to March), aboard the ice breaker Polarstern. The research vessel Polarstern drifted with the pack ice in the central Arctic mainly at latitudes >85°N during the winter half year. The cirrus statistics show typical properties of ice clouds of the synoptic cirrus category (top-down generation of cirrus structures). The ice clouds mostly started to evolve at heights close to the tropopause. Cirrus top temperatures accumulated between −60 and −75°C. The cirrus optical thickness (COT at 532 nm) of the ice clouds covered a wide range of values from <0.03 (subvisible cirrus fraction, 25% out of all cases) over 0.03–0.3 (visible thin cirrus, 40%) to >0.3 (opaque cirrus fraction, 35%). In about 30% out of all high altitude lidar observations, cirrus signatures were detected,

much more than expected (10%). This fact may be taken as a first hint that wildfire smoke was significantly involved in Arctic cirrus formation. The smoke particle surface area concentration around the tropopause was of the order of 5-15 μm^2 cm^{-3}

and indicated considerably enhanced levels of aerosol pollution in the upper troposphere. Based on the combined lidar-radar measurements, we analyzed 20 cirrus cases in terms of profiles of the ice water content (IWC), ice crystal number concentration (ICNC), and visible extinction coefficient. IWC mostly ranged from 0.001-0.01 g/m^{-3} and ICNC (in the ice virga) accumulated in the range from 0.01 to 10 L^{-1}. Three facts (in combination) corroborate our hypothesis that aged wildfire smoke triggered ice formation in many of the observed cirrus systems: (1) The low ICNC values point to heterogeneous ice nucleation, (2) the

elevated smoke pollution levels (in terms of particle surface area concentrations) were high enough to significantly influence ice nucleation in the upper troposphere, and (3) the high ice saturation ratios accumulating around 1.3-1.4 in the upper part of the observed and analyzed cirrus decks indicate quite inefficient INPs as expected in the case of organic aerosol particles (wild fire smoke particles).

1 Introduction

A significant increase in the occurrence frequency of wildfire smoke layers in the upper troposphere and lower stratosphere (UTLS) has been observed in the northern hemisphere since 2017 (Baars et al., 2019; Ohneiser et al., 2021; Trickl et al., 2024). The increase may be linked to climate change (Jolly et al., 2015; Abatzoglou et al., 2019; Kirchmeier-Young et al., 2019; **?**). In order to adequately consider smoke particles in atmospheric modeling, the role of wildfire smoke in the climate system and respective impact pathways need to be explored in detail. A relevant, climate-sensitive pathway is ice formation in the

upper troposphere (Lohmann and Neubauer, 2018). Two ice nucleation modes have to be distinguished, heterogeneous ice nucleation on solid surfaces of ice-nucleating particles (INPs) and homogeneous ice nucleation of liquid background aerosol particles (sulfate particles). Heterogeneous ice nucleation starts at lower ice saturation ratios than homogeneous freezing and leads to relatively low values of the ice crystal number concentration (ICNC) of typically <50 L^{-1} in contrast to ICNC value of the order of 500 L^{-1} in the case of homogeneous freezing (see, e.g., Kärcher et al., 2022), and to larger ice crystal sizes.

The mechanism by which a cirrus cloud forms determines the impact on the radiation field and seeder-feeder and precipitation features (DeMott et al., 2010) and thus needs to be considered in weather and climate models (Lynch et al., 2002; Heymsfield et al., 2017). During the one-year MOSAiC (Multidisciplinary drifting Observatory for the Study of Arctic Climate) expedition (Shupe et al., 2022), we observed a large number of cirrus systems developing in the wildfire-smoke-polluted upper troposphere over the central Arctic.

Clear evidence for the ability of aged wildfire smoke particles (organic particles) to initiate heterogeneous ice nucleation was recently provided by Mamouri et al. (2023). A first MOSAiC (Multidisciplinary drifting Observatory for the Study of Arctic Climate) case study of smoke-cirrus interaction was discussed by Engelmann et al. (2021). In this part 1 of a series of two articles, we present an extended analysis of the entire MOSAiC data set. Goal of our MOSAiC cirrus studies is to provide observational evidence for a dominating impact of aged wildfire smoke (organic aerosol particles) on cirrus formation in the central Arctic during the winter half year of 2019-2020. Aim of the simulations, presented in part 2, is to gain a more detailed

insight into the potential smoke influence on ice nucleation at the observed environmental and meteorological conditions (temperature, relative humidity) and by considering realistic gravity wave characteristics (updraft speed, wave amplitudes). Vertical movements, i.e., adiabatic lofting of air parcels are essential to initiate ice nucleation. For the first time state-of-the-art remote sensing of aerosol and cirrus properties is closely combined with comprehensive modeling of cirrus evolution processes
60   to explore aerosol-cirrus interaction.

The MOSAiC smoke and cirrus observations were performed with lidar and radar instruments (Engelmann et al., 2021) aboard the German research ice breaker Polarstern (Knust, 2017). The wildfire smoke originated from record-breaking forest fires in central and eastern Siberia in the summer of 2019 (Ohneiser et al., 2021; Ansmann et al., 2024b). The aerosol pollution spread all over the Arctic in August 2019 (Xian et al., 2022a, b) and reached even the lower stratosphere where the aerosol
65   particles contributed to polar ozone depletion in the spring of 2020 (Ohneiser et al., 2021; Voosen, 2021; Ansmann et al., 2022). The UTLS wildfire smoke layer was observable until May 2020 at high northern latitudes.

The Polarstern was trapped in the pack ice and drifted through the Arctic Ocean from 4 October 2019 to 16 May 2020, mostly at latitudes >85-86°N. A multiwavelength Raman polarization-sensitive lidar and a 35 GHz cloud radar of the ARM (Atmospheric Radiation Measurement) mobile facility 1 (AMF-1) were continuously operated (around the clock) side by side
70   to collect tropospheric and stratospheric aerosol and cloud profile data up to 30 km height throughout the entire expedition period. Accompanying radiosondes, launched every 6 hours, provided dense sets of observations of the atmospheric state in terms of temperature, relative-humdity, and wind profiles (Maturilli et al., 2021, 2022).

Smoke particles (or more general, organic aerosol particles) seem to be not very efficient INPs (Knopf et al., 2018; Knopf and Alpert, 2023). However, they can influence ice nucleation in very different ways. If the particles are in a glassy state, they
75   can act as INPs in deposition ice nucleation (DIN) processes (Murray et al., 2010; Wang and Knopf, 2011; Wang et al., 2012). DIN is defined as ice formation occurring on the INP surface by water vapor deposition from the supersaturated gas phase. When the smoke particles can take up water and a liquid surface around the particles develops, immersion freezing can proceed (Wang et al., 2012; Knopf and Alpert, 2013; Knopf et al., 2018). According to classical nucleation theory and observations, DIN INPs are expected to be more efficient in warm cirrus with cloud top temperatures around $-50°C$ than in cold cirrus with
80   top temperatures of $-70°C$ (Trainer et al., 2009; Pruppacher and Klett, 2010; Alpert et al., 2011; Wang and Knopf, 2011; Wang et al., 2012; Primm et al., 2017). The onset ice supersaturation $S_{i,on}$ decreases with increasing temperature. Strong, burst-like ice nucleation sets in for $S_i > S_{i,on}$. This aspect is shown in the simulation study (part 2). Because of the complex chemical, microphysical, and morphological properties of aged fire smoke particles the development of smoke INP parameterization schemes is generally a crucial task (Knopf et al., 2018).
85   The particles and released vapors in biomass burning plumes undergo chemical and physical aging processes on their way up to the tropopause and during long-range transport over weeks and months. These aging processes change the chemical composition of the smoke particles, their morphological characteristics (size, shape, and internal structure), and the internal mixing state of the smoke particles. After finalizing the aging process, the smoke particle may show a core-shell structure with a BC-containing core (few percent of BC) and an OC-rich shell (OC for organic carbon), and that the ability to serve as INP
90   mainly depends on the material in the shell and thus on the organic material of the particles. Biomass-burning particles also
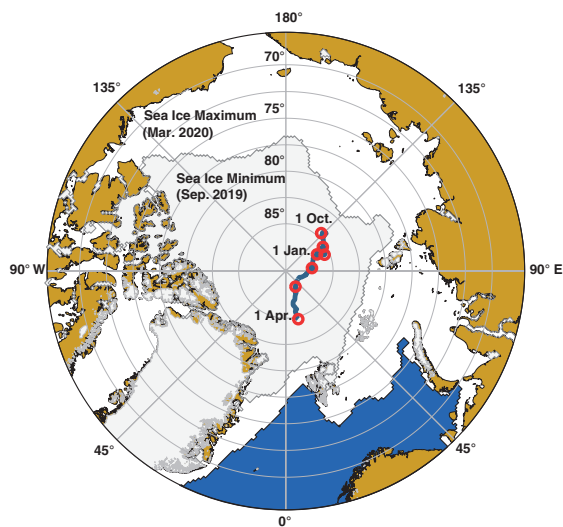
Figure 1. Drifting route of the ice breaker Polarstern from 1 October 2019 to 1 April 2020. Each of the eight red circles marks the beginning of the next month. The map was produced with 'ggOceanMaps' (Vihtakari, 2020) by using Sea Ice Index Version 3 data (Fetterer et al., 2017).

contain humic-like substances which represent large macromolecules that could serve as INP at low temperatures of -50 to $-70°$C (Kanji et al., 2008; Wang and Knopf, 2011; Wang et al., 2012; Knopf et al., 2018). Jahn et al. (2020) and Jahl et al. (2021) hypothesized that aged smoke particles contain minerals and that these components may determine the smoke INP efficacy.

95   The article is organized as follows. In Sect. 2, the field campaign, used instrumentation (lidar, radar, disdrometer, radiosonde) and applied lidar and radar data analysis methods (lidar retrievals of cirrus optical properties and INP profiles, combined lidar-radar retrievals of height profiles of ICNC and ice water content) are outlined. The key findings of our MOSAiC cirrus studies (cirrus statistical analysis, discussion of case studies in terms of optical and microphysical properties) are presented in Sect. 3. Sect. 4 provides a short summary and concluding remarks.

2 Polarstern cruise, remote sensing, radiosonde and disdrometer instrumentation, and observational products

The MOSAiC expedition began end of September 2019 and lasted until the beginning of October 2020. In this article, we focus on the cirrus observations during the winter half year from 1 October 2019 to 31 March 2020. Figure 1 shows the track of the drifting Polarstern from 1 October 2019 to 16 May 2020. Each of the red circles along the Polarstern track indicates the beginning of a new month. Most of the time the observations were performed between $85°$ and $88.5°$N during the first six months of the MOSAiC campaign.
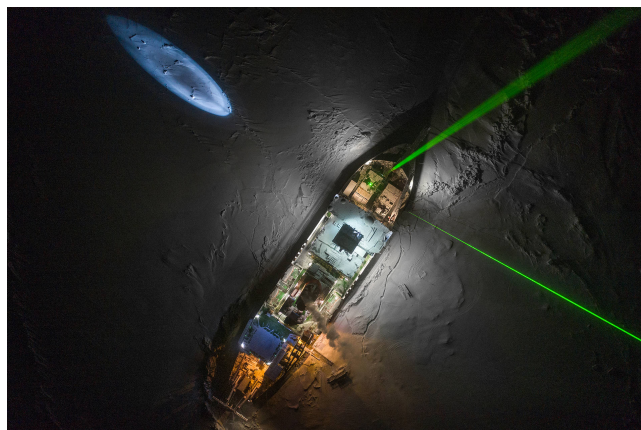
Figure 2. Drone-based photograph of Polarstern, drifting with the pack ice, along the route shown in Fig. 1. The two green laser beams are produced by the ARM lidar (left beam, exactly vertically pointing) and the TROPOS lidar (right beam, 5° off-zenith beam pointing to avoid strong specular reflection by falling, preferably horizontally aligned ice crystals). The picture was taken by Jakob Stark and shown within the Geo journal report of Esther Horvath (https://geo.pageflow.io/gefangen-im-eis#240143, authorship: Alfred-Wegener-Institut / Esther Horvath and Jakob Stark (CC-BY 4.0))

The remote sensing instrumentation aboard Polarstern mainly consisted of the Atmospheric Radiation Measurement (ARM) mobile facility AMF1 of the US Department of Energy (http://www.arm.gov, last access: 22 January 2024) and the OCEANET-Atmosphere container of the Leibniz Institute for Tropospheric Research (TROPOS) (Engelmann et al., 2016). These containers were deployed on the bow (front deck) of the Polarstern. Photographs of the main ship-based MOSAiC atmospheric measure-
110 ment platforms aboard Polarstern are shown in Fig. 3 in Shupe et al. (2022) and Fig. 2 in Engelmann et al. (2021).

Two lidars transmitting laser beams at 532 nm (visible green light) into the atmosphere were operated continuously aboard Polarstern throughout the one year expedition. Figure 2 shows the two beams above Polarstern. The picture was taken with a drone overflying Polarstern on 31 October 2019.

2.1 Polly lidar

115 The multiwavelength polarization Raman lidar Polly (POrtabLe Lidar sYstem) (Engelmann et al., 2016) performed measure-ments from 26 September 2019 to 2 October 2020 (Polly, 2024). A detailed description of the Polly instrument can be found in Hofer et al. (2017) and Jimenez et al. (2020). The basic aerosol observations comprise height profiles of the particle backscat-ter coefficient at 355, 532, and 1064 nm, the particle extinction coefficient at 355 and 532 nm, the respective extinction-to-backscatter ratio (lidar ratio) at 355 and 532 nm, and the particle linear polarization ratio at 355 and 532 nm (Baars et al., 2016;
120 Hofer et al., 2017; Ohneiser et al., 2021). The retrieval of smoke microphysical properties is outlined in Ansmann et al. (2021) and Ansmann et al. (2023). By means of the measured upper tropospheric smoke backscatter coefficients, the particle surface area concentration (PSAC), the mass concentration, and the number concentrations n_{50} and n_{250} considering particles with radius >50 nm and >250 nm, respectively, can be estimated. PSAC is the aerosol input in the retrieval of the DIN INP number

concentration for organic particles (Wang and Knopf, 2011). n_{250} is interpreted as the reservoir of potential INPs. More details

125   to the conversion of optical into microphysical properties is given in Sect. 3.2. The data analysis regarding the microphysical

properties of ice crystals is described in Sect. 2.3.

2.2   ARM cloud radar

We used the 35 GHz cloud Doppler radar measurements (Ka-band ARM Zenith Radar, KAZR) of the ARM (Atmospheric

Radiation Measurement) mobile facility 1 (AMF-1) (ARM, 2024). KAZR measures the radar moments, including reflectivity,

130   mean Doppler velocity, and spectrum width, which provide insight into the mass, size, and fall speed of cloud and precipitation

particles (Shupe et al., 2022). Additionally, the vertically pointing radar recorded the full Doppler spectrum, which offers

further insight into the cloud particle populations and processes.

2.3   Cirrus-related data analysis

The classical Raman lidar technique is used to obtain cirrus optical properties (Ansmann et al., 1992). In the determination of

135   the backscatter coefficient at 532 nm, no assumption of the extinction-to-backscatter ratio (lidar ratio) is required. Furthermore,

the solutions are not affected by any multiple scattering effect. After multiplication of the backscatter coefficients with a typical

single-scattering lidar ratio of 32 sr at 532 nm, the desired cirrus extinction coefficient profile is revealed. The 532 nm cirrus

lidar ratio is in the range of 28-35 sr (Seifert et al., 2007; Giannakaki et al., 2007; Garnier et al., 2015; Josset et al., 2012; Haarig

et al., 2016; Voudouri et al., 2020). Integration from cirrus base to top height yields the 532 nm cirrus optical thickness. To

140   avoid a strong bias in the extinction profiles caused by specular reflection by horizontally oriented falling ice crystals Thomas

et al. (1990) the laser beam was directed to an off-zenith angle of 5°. In the case of zenith-pointing lidars the backscatter and

extinction coefficients and related cirrus optical thickness can be easily overestimated by a factor of 10. More details to this

problem can be found in Mamouri et al. (2023).

    An automated (unsupervised) data analysis was applied to the entire MOSAiC lidar data set collected from 1 October 2019

145   to 31 March 2020. In the first step, we calculated 1 hour mean signal profiles. About 4300 1-hour profiles are theoretically

possible within 180 days. We obtained 1716 1-hour profiles showing atmospheric backscatter up to the stratosphere. These

profiles were not influenced by low-level clouds and fog and could thus be considered in the cirrus statistics. Further 220

2-hour mean signal profiles could be considered in the cirrus statistics. A longer averaging period was necessary in these cases

because of the low signal-to-noise ratio in the case of respective 1-hour profiles. All in all, 1936 lidar profiles were available

150   for further use. 30% of these profiles showed cirrus signatures (652 hours, 587 profiles).

    The following criteria were applied to identify cirrus layers and to determine base and top heights of the cirrus layer.

First of all we checked the radiosonde profile of the temperature and restricted the cirrus identification to heights above the

−28°C temperature level. Then we used two criteria to identify the cirrus layer. The volume depolarization ratio must exceed

coherently (over a vertical range >300 m) the 10% level and, at the same time, the particle backscatter coefficient must exceed

155   0.1 Mm^{-1} sr^{-1}. Identified cirrus layers with a vertical depth of <300 m were thus reject. Since the majority of ice clouds

formed in the uppermost part of the troposphere we included the tropopause information from the radiosonde observations in

our cirrus studies. The tropopause height was determined following the NASA procedure described in Ohneiser et al. (2021). The results of the cirrus statistical analysis are presented and discussed in Sect. 3.1.

2.4 ICNC and IWC retrieval

160 The retrieval of the ice crystal number concentration ICNC and of the ice water content IWC is based on the synergy of 35 GHz KAZR and 532 nm backscatter lidar observations. The LIRAS-ice (LIdar RAdar Synergy - retrieval of ICE microphysical properties) analysis scheme (Bühl et al., 2019) was originally developed to investigate the impact of Saharan dust on mixed-phase and ice clouds over the Eastern Mediterranean (Ansmann et al., 2019).

LIRAS-ice makes use of the measured profiles of the radar reflectivity factor Z (8.5 mm wavelength) and of the cirrus (single 165 scattering) particle extinction coefficient E at 532 nm wavelength. A careful and accurate determination of the E profile is of fundamental importance for a trustworthy inversion of the combined radar-lidar observations. The optimum, most robust E profiles are obtained by means of the Raman lidar method described in Sect. 2.3.

During the MOSAiC expedition, high quality cloud radar observations were possible in cirrus virga, only. The estimation of microphysical properties of ice particles was thus restricted to the lower part of the cirrus system. The applied numerical 170 inversion technique of Bühl et al. (2019) is based on a look up table (LUT) which contains the properties of the particle size distribution PSD (assumed to be a monomodal gamma size distribution) (Hogan et al., 2003; Sekelsky et al., 1999; Ulbrich, 1983) and values of Z and E. PSD (i.e., the ice crystal number concentration $N(D)$ as function of diameter D), Z, and E are computed with Eqs. (1), (2), and (5) in Bühl et al. (2019), respectively. PSD is a function of the median particle maximum diameter D_m and the shape parameters μ (describing the tilt of the gamma size distribution). More details are given below. In 175 our MOSAiC related modeling effort (LUT computations) we follow Bühl et al. (2019): Z is a function of crystal particle mass (Eq. (B1) with parameters $\alpha = 0.012$ and $\beta = 2.4$ in the case of the MOSAiC data analysis. E depends on the crystal surface area or geometrical cross section (Eq. B2) with parameters $\gamma = 0.17$ and $\sigma = 1.8$). The parameters α, β, γ and σ are given in Tables A1 and A2 in Bühl et al. (2019). For the crystal shape assumption (defined in Table A2) we assume hexagonal plates for the diameter range from 15 to 100 μm and an aggregate mixture for the sizes from 600 μm to 5 mm.

180 The ice crystal diameter range from 100 μm to 5 mm is considered in the inversion procedure. This assumption reflects realistic characteristics of the crystal size distribution in (aged) ice crystal virga in the case of the synoptic cirrus category (Lynch et al., 2002). The number concentration and size of the crystals in the virga depend on ice crystal growth and collision and aggregation processes. Nucleation of new ice crystals and thus a potential occurrence of a second mode in the size distribution can be ignored at relative humidity over ice of around 100% (i.e., in the absence of strong ice supersaturation) as 185 typically observed with MOSAiC radiosondes in the cirrus virga. The assumption of a monomodal gamma size distribution of the crystals is in agreement with other Arctic cirrus observations (Wolf et al., 2018, 2019; De La Torre Castro et al., 2023). In Sect. 3.4, we will show a comparison with disdrometer-derived ICNC values that corroborate that our approach is fully justified. Our extended sensitivity analysis revealed that the selected size range (e.g., from 10, 25, or 100 μm up to 5000 μm) does not play a role in the ICNC retrieval when assuming a monomodal gamma size distribution for the well developed crystal 190 size distributions in ice virga.

Table 1. Overview of Polly observational products, used in this study, and typical relative uncertainties in the determined and retrieved properties. r denotes aerosol particle radius.

Smoke and cirrus properties	Uncertainty
Cirrus top height, depth [m]	$< 1\%$
532 nm cirrus backscatter coef. $[\text{Mm}^{-1}\,\text{sr}^{-1}]$	$\leq 5\%$
532 nm cirrus extinction coefficient $[\text{Mm}^{-1}]$	$\leq 15\%$
532 nm cirrus optical depth	$\leq 10\%$
Smoke particle surface-area conc. $[\mu\text{m}^2\,\text{cm}^{-3}]$	$\leq 25\%$
Smoke particle number conc. ($r > 250$ nm) $[\text{cm}^{-3}]$	$\leq 25\%$
Ice nucleating particle number concentration $[\text{L}^{-1}]$	Order of magn.
Ice crystal number concentration $[\text{L}^{-1}]$	Order of magn.

In the next step, we estimated the median diameter D_{m} of the PSD from Z and Z/E by comparison with simulated cloud radar spectra and lidar parameters (stored in the LUT). A fixed shape parameter of $\mu = 2$ of the gamma size distribution is used (Eq. (1) in Bühl et al. (2019)). Finally, we scaled the results with the observed values of E to obtain ICNC and IWC profiles. The main goal of the retrieval is thus to find a PSD that leads to the same variables as the measured ones (Z, E). The method developed by Bühl et al. (2019) was well tested and applied to cirrus observations over the Eastern Mediterranean (Ansmann et al., 2019).

We applied the recently published CAPTIVATE (Cloud, Aerosol and Precipitation from mulTiple Instruments using a VAri- ational TEchnique) algorithm (Mason et al., 2023) to the combined MOSAiC lidar-radar cirrus data sets as well. We found in general good agreement between our LIRAS-ice and the CAPTIVATE results for IWC. However, the ICNC solutions deviate because the ICNC retrieval is rather sensitive to the lidar and radar input data and assumptions on the crystal shape character- istics. CAPTIVATE uses the directly measured attenuated backscatter coefficients (i.e. calibrated range-corrected backscatter signals) as input and derives the required single scattering extinction coefficients as part of the data analysis. Our experience with CAPTIVATE shows that the estimation of the single scattering extinction profile can be a source of significant uncertainty.

As discussed in Bühl et al. (2019), the uncertainty in the ICNC estimation is roughly characterized by a factor of 3 (around the most reasonable solution). Thus, LIRAS-ice allows us to determined the order of magnitude of occuring ICNC in cirrus fall strikes. This uncertainty margin holds in general for all ICNC radar-lidar retrievals. Table 1 provides an overview about the uncertainties in the observed and retrieved aerosol and cirrus products.

2.5 Two-dimensional video disdrometer (2DVD)

The two-dimensional video disdrometer (2DVD) is a ground-based precipitation gauge which detects single precipitation particles within a certain measuring area (Kruger and Krajewski, 2002; Gaudek, 2024). The 2DVD was originally designed to measure rain drop size distributions. The investigation of solid hydrometeors with such devices has rather been subject of

research in recent years. The instrument was developed by Joanneum Research, Graz, Austria (https://www.joanneum.at/). During the MOSAiC expedition it was operated on the roof of the TROPOS OCEANET-Atmosphere container. The 2DVD, including a product characterization, is described in detail in Gaudek (2024).

215   The 2DVD allowed us to measure ICNC on a calm day (23 November 2019) and to compare the values with respective numbers from the lidar-radar retrieval. Furthermore, the 2DVD observations provided information on the ice crystal sizes, terminal velocities of ice crystals, and whether the ice crystals were compact or rather complex in shape and thus hints on the importance of crystal collision and aggregation processes.

2.6   Polarstern radiosonde

220   Vaisala radiosondes (type RS41) were launched regularly every 6 hours throughout the entire duration of MOSAiC, including periods when Polarstern was in transit (Maturilli et al., 2021, 2022). The radiosondes provide vertical profiles of temperature, relative humidity, pressure, and winds from 12 m (the altitude of the helideck from which they were launched) up to an altitude of about 30 km, thus covering both troposphere and lower stratosphere (Shupe et al., 2022). Quality control for appropriate physical ranges has been applied.

3   Observations

The MOSAiC observations and retrieval products are presented and discussed in several subsections. In Sect. 3.1, we begin with the results of a statistical anlysis of observed cirrus geometrical and optical properties. In Sect. 3.2, we briefly summarize the aerosol conditions at tropopause level where ice formation usually started. A detailed discussion on Arctic aerosols from the surface to the tropopause was given in Ansmann et al. (2023). In Sect. 3.3 and 3.4, we present our findings regarding the

230   microphysical properties of 12 cirrus systems (20 profile data sets) observed in the winter months (November 2019 to February 2020).

3.1   Cirrus statistics for the winter half year 2019-2020

Figure 3 presents the statistical results of the cirrus observations from 1 October 2019 to 31 March 2020. Although the observations cover the winter half year only the comparison with other studies (discussed below) suggest that they are representative

235   for the entire year. During the summer half year, less than 30 cirrus events (one hour mean cirrus profiles) could be collected. Low clouds and fog prohibited upper tropospheric measurements most of the time during spring and summer months. According to the cirrus classification of Lynch et al. (2002) all of the observed Artic cirrus clouds belong to the synoptic cirrus category (top-down generation of cirrus structures). Ice nucleation starts at cloud top, where usually the highest values of the ice saturation ratio are observed and later on extended virga of falling ice crystals evolve, and reach lower and lower heights. An

240   example is discussed in the next section. De La Torre Castro et al. (2023) reported that 86% of the cirrus layers they observed during a summer campaign in June and July 2021 at latitudes from 60-76°N belonged to the synoptic cirrus category. 14% of the ice clouds were orographically induced cirrus or anvil cirrus.
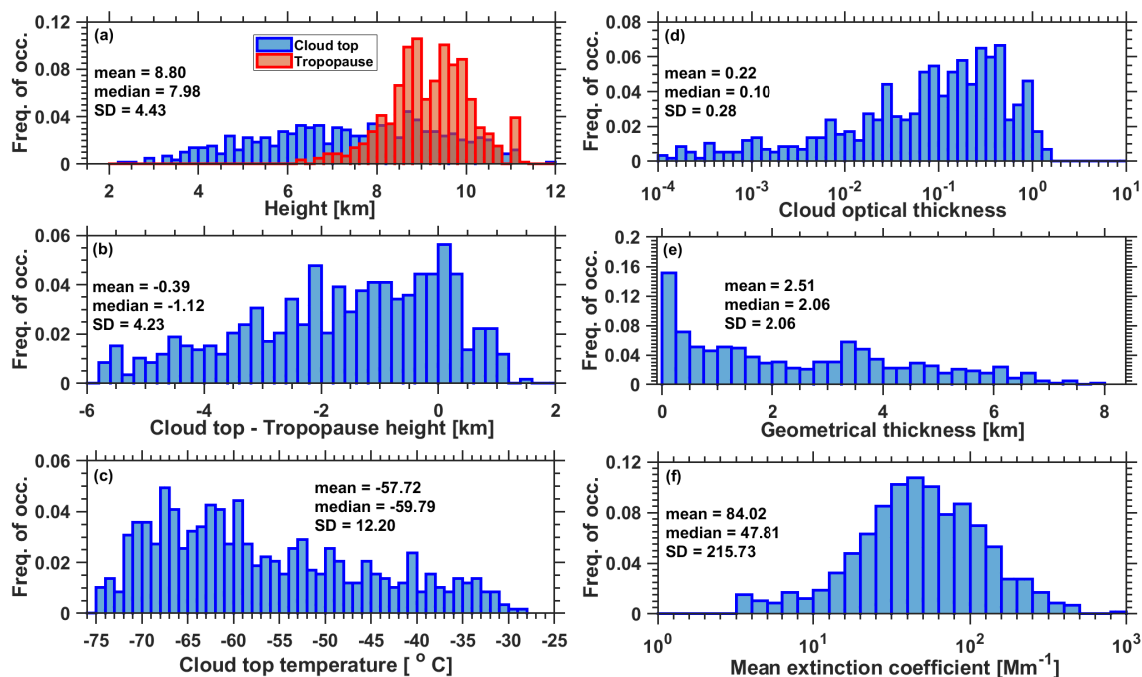
Figure 3. MOSAiC cirrus statistics considering all available lidar observations from 1 October 2019 to 31 March 2020. The normalized frequency of occurrence is shown. (a) Cirrus top height and tropopause, (b) Vertical distance of the cirrus top height from the tropopause, (c) cirrus top temperature, (d) cirrus optical thickness (corrected for multiple scattering), (e) cirrus vertical extent (from top to virga base height), and (f) cirrus mean extinction coefficient (corrected for multiple scattering). Median, mean, and SD values are given as numbers.

As mentioned in Sect. 2.3, the MOSAiC cirrus statistics in Fig. 3 is based on 1716 1-hour mean and 220 2-hour mean signal profiles. They cover 2156 hours and thus almost 50% of the theoretically possible 4320 1-hour profiles of a half year. All

245 profiles showing cirrus signatures and cloud top temperatures <-28°C are considered in the shown statistics. In more than 90% out of all cases the cirrus top temperature was <-40°C.

The main findings can be summarized as follows: More than 30% out of all profiles showed cirrus signatures (652 hours, 587 profiles). Typical cirrus occurrence frequency is of the order of <10% according the space lidar observation with CALIOP (Cloud-aerosol lidar with orthogonal polarization) at latitudes around 80°N in 2006-2007 (Sassen et al., 2009; Heymsfield

250 et al., 2017). Most cirrus clouds developed at or close to the tropopause. The tropopause height distribution is shown in panel a in Fig. 3. Many detected cirrus features far below the tropopause are related to remaining and dissolving virga structures. Most ice nucleation occurred at temperatures from −60 to −75°C. The values for the cirrus optical thickness accumulate in the range from 0.05 to 0.5. The broad distribution of cirrus vertical depth indicates the strong impact of virga structures and the strongly varying virga base height. The cirrus mean extinction coefficient shows a Gaussian distribution (in logarithmic scales)

255 with typical extinction values from 30 to 300 Mm^{-1}.

Sassen and Cho (1992) classified cirrus clouds as subvisible cirrus when the cirrus optical thickness COT is <0.03, as visible cirrus when the COT ranges from 0.03-0.3, and as opaque cirrus when COT>0.3. According to this classification, 25% of the observed central Arctic cirrus clouds were subvisible, 40% visible, and 35% opaque cirrus. Heymsfield et al. (2017) stated that typical cirrus top temperatures are between −60 and −73°C. Cirrus frequency of occurrence was stated to be, on average, 7%
260 in the central Arctic (Sassen et al., 2009; Heymsfield et al., 2017). Top heights from 8-14 km for Arctic cirrus, mentioned by Heymsfield et al. (2017), are mainly based on the studies of Sassen et al. (2008, 2009). Schäfer et al. (2022) analyzed ground-based lidar observations at the ALOMAR site in northern Norway (69.1°N) and compared the findings with respective results from CALIOP overflights (2011-2017). Typical cirrus top temperatures were in the range of 210-220 K (fall, winter) and 220-230 K (spring, summer). Cirrus top was mostly at heights from 8.5-10.5 km. Cirrus base heights ranged from 4-11 km over the
265 ALOMAR lidar site. Nakoudi et al. (2021) analyzed lidar data collected over Ny Ålesund, Svalbard, Norway (78.6°N) from 2011-2020, and also found cirrus top heights mainly between 8.5 and 10.5 km (throughout the year). Cirrus top temperatures accumulated between -60 and -70°C. Voudouri et al. (2020) analyzed long-term observations (2011-2016) in Finland (Kupio, 62.7°N). Cirrus top heights were mostly between 9 and 10 km in winter and 10-10.5 km in summer. Mean COT at 532 nm was found to be 0.24±0.2, with 3% contributing to the subvisible cirrus fraction, 71% to the visible cirrus fraction, and 26% to the
270 opaque cirrus fraction. These numbers are very different from the MOSAiC values of 25% subvisible, 40% visible, and 35% opaque ice clouds.

The statistical results in Fig. 3 do not provide any hint whether homogeneous or heterogeneous ice nucleation or both processes were responsible for the formation of ice clouds. To obtain a more specific insight into the ice nucleation processes we need to gain information about the microphysical properties by means of combined lidar-radar observations, especially
275 about ICNC in the cirrus top layers and the virga zones since low ICNC values are indicative for heterogeneous ice nucleation and high ICNC numbers for homogeneous ice nucleation (Kärcher et al., 2022).

3.2 Upper tropospheric aerosol conditions during the winter 2019-2020

Multiwavelength lidar and sunphotometer observations show that the particle size distribution of aged wildfire smoke particles can be characterized by an accumulation mode which is shifted to larger particle sizes (Ansmann et al., 2021; Ohneiser et al.,
280 2021). The mode radius increases from about 130-150 nm to 250-400 nm during long-range transport. The measured optical properties can be used to estimate particle number concentrations n_{50} and n_{250}, i.e., particles with radius $r > 50$ nm and $r > 250$ nm, respectively, and particle surface area concentration (PSAC), volume, and mass concentrations (Ansmann et al., 2021). The uncertainty in the retrieval products is of the order of 25% in the case of n_{250} and PSAC (see Table 1).

During the MOSAiC winter half year the upper troposphere was significantly polluted by aged Siberian wildfire smoke
285 (Ohneiser et al., 2021; Ansmann et al., 2023). In Fig. 4, the observed ice-nucleation-relevant particle surface area concentration (PSAC) of the smoke particles is shown. These data are used as input in the INP parameterization within the simulation studies in part 2 (Ansmann et al., 2024a). The corresponding particle number concentrations n_{50} and n_{250} may be regarded as INP reservoirs, containing all particles that can eventually be activated as INPs (Knopf et al., 2023). This aspect is further discussed by Knopf et al. (2023). PSAC of 10 μm^2 cm^{-3} corresponds to n_{250} of about 2000 L^{-1} and n_{50} of 50000-100000 L^{-1}.
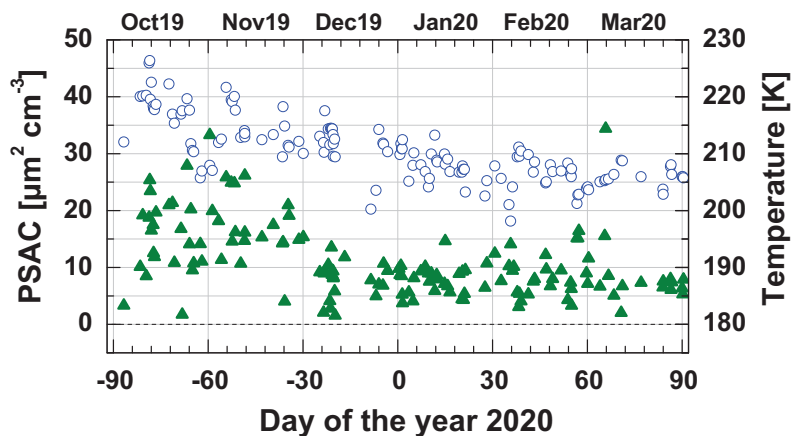
Figure 4. Smoke particle surface area concentration (PSAC) values (for the tropopause height level, green triangles) together with tropopause temperatures (open blue circles) from the beginning of October 2019 to the beginning of April 2020. The lidar observations were performed during cirrus-free periods.

According to Schröder et al. (2002) the liquid background sulfate particle number concentration, i.e., the INP reservoir in the case of homogeneous freezing processes, is of the order of 250 cm^{-3} (or 250000 L^{-1}) in the upper troposphere. The respective particle volume concentration of around 1 μm^3 cm^{-3} serves as aerosol input in homogeneous ice nucleation computations (Koop et al., 2000). In terms of optical properties, the MOSAiC smoke 532 nm extinction coefficients in the UTLS height range were with 3-5 Mm^{-1} about a factor of 20 higher than respective extinction coefficients for the UTLS background sulfate aerosol of 0.1-0.25 Mm^{-1} (Jäger, 2005; Baars et al., 2019).

As can be seen in Fig. 4, the pollution level did not change much with time, especially during the main winter months from December to March. The PSAC values accumulated in the range from 5-15 μm^2 cm^{-3}. A rather strong and long-living polar vortex controlled the weather and vertical and horizontal aerosol transport conditions from the end of December 2019 to May 2020. A depletion of the smoke particle reservoir by permanent cirrus formation is not visible. The tropopause temperatures decreased on average from November 2019 to March 2020.

3.3 22 January 2020 cirrus case study

To obtain more insight into the basic cirrus formation processes and the potential impact of smoke particles on ice nucleation, we need to proceed towards the retrieval of ICNC and IWC. By combining lidar and radar measurements the microphysical properties of ice clouds can be estimated as outlined in Sect. 2.5. We applied the LIRAS-ice method to many cirrus events observed from November 2019 to February 2020. We start with a typical cirrus life cycle, highlighted in Fig. 5. The measurement was performed on 21-22 January 2020 at 87.5°N. From 21 January, 12 UTC, to 26 January, 20 UTC, cirrus and virga formation continuously occurred over Polarstern. Ice nucleation was initiated mainly at heights >10 km and at temperatures of −70 to −74°C. The ice particles grew fast by water vapor deposition on the available crystal surfaces and began to fall. According to
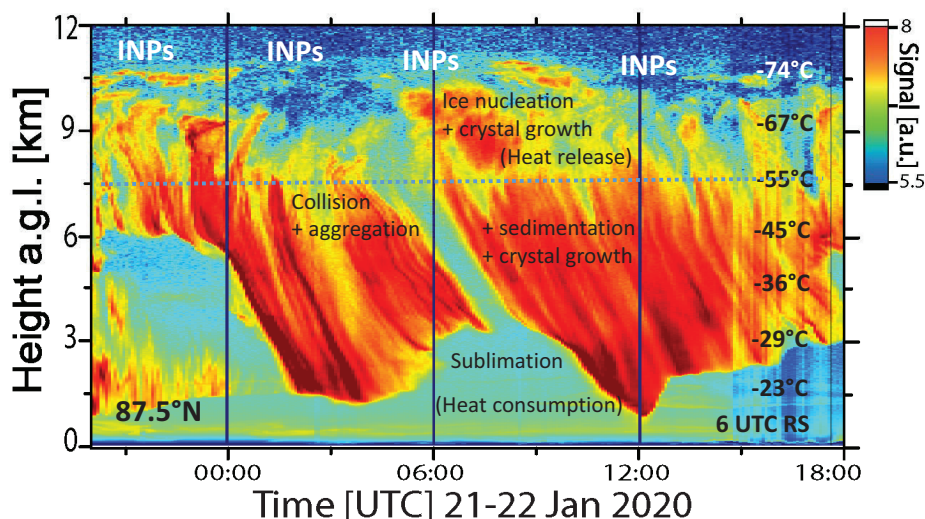
Figure 5. Life cycles of two cirrus systems, the first one from about 21 UTC on 21 January to 7 UTC on 22 January, and the second one from 6 UTC to 16 UTC on 22 January 2020. Cirrus structures are mainly given in yellow and red colors. The Polarstern lidar observation (in terms of the calibrated range-corrected 1064 nm backscatter signal) was performed at 87.5°N. The cirrus clouds belong to the synoptic cirrus category (top down generation of cirrus structures). Cirrus generation cells were mainly above 9 km height, the virga zone extended from about 9 km down to 1 km above Polarstern. Temperatures (given as numbers on the right side) were measured with 6 UTC radiosonde. The vertical black lines indicate 0, 6, and 12 UTC radiosondes (launched at 23, 5, and 11 UTC, respectively). All relevant processes are indicated such as nucleation, growth, sedimentation, and aggregation. The blue dotted line shows the maximum height up to which cloud radar reflectivity is available to retrieve microphysical properties. Smoke particle INPs showed a maximum at the tropopause level around 10.5-11 km height.

Bailey and Hallett (2004, 2012) crystals grow by 0.01-0.05 μm s^{-1} (diameter growth per second) at temperatures from -50
310 to -30°C and ice supersaturation levels around 1.1 as given on 22 January 2020 in the main virga zone between 3 and 7 km height. The falling ice crystals formed long virga structures. In the case of the virga between 1.5 and 7.5 km height, observed from 8-12 UTC on 22 January, crystals probably grew to sizes of 150-750 μm in these 14400 s by water vapor deposition on the crystals. During sedimentation, the crystals reach warmer air and grow faster (at given, almost constant ice supersaturation conditions) because the growth rate increases with temperature (Bailey and Hallett, 2004, 2012). Different crystal nucleation
315 times and different growth rates at different heights and temperatures lead to a broad spectrum of ice crystal sizes. The resulting fall speed spectrum foster collision and aggregation processes and may lead to a considerable number of crystals with diameters exceeding even 1 mm in the lower half of the virga before evaporation of the crystals in the lowest part of the virga start to dominate.

The ice particles moved downward from heights of 7.5 km to 1.5 km during the 4-hour virga event from 8-12 UTC and thus
320 with a mean falling speed of 40 cm s^{-1}. The Doppler radar observations indicated falling velocities around 50 cm s^{-1}.
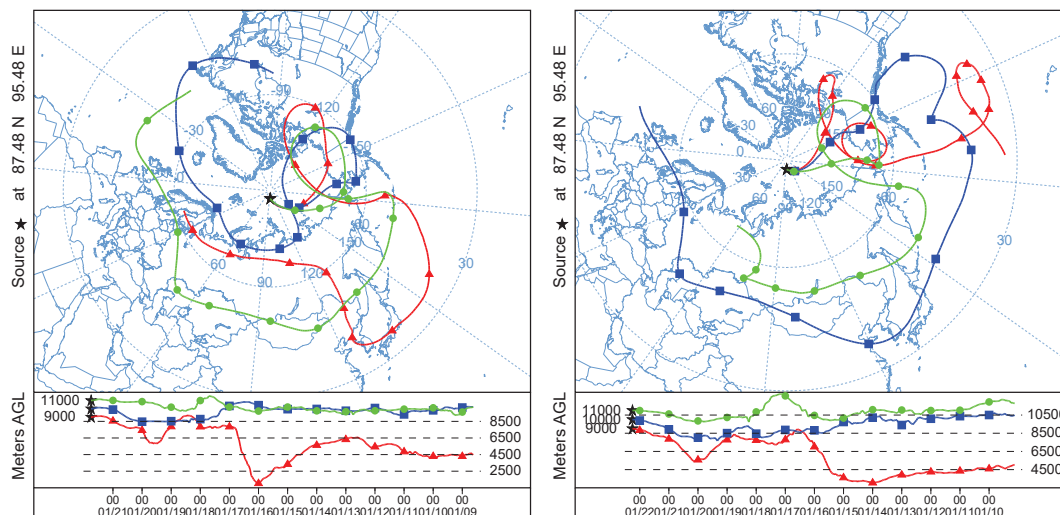
Figure 6. HYSPLIT 10 day backward trajectories, arriving over Polarstern (indicated by a star) on (a) 21 January 2020, 18:00 UTC and (b) on 22 January 2020, 6:00 UTC (HYSPLIT, 2024; Stein et al., 2015; Rolph et al., 2017). Arrival heights are at 9000 m (red), 10000 m (blue), and 11000 m (green).

According to the HYSPLIT backward trajectories in Fig. 6 the humid air mass, in which the cirrus formed, originated from the Pacific Ocean. The air mass spent 4-5 days in the polluted upper troposphere over the Arctic before cirrus began to form on 21 January 2020. During these 4-5 days there was sufficient time for entrainment of aged wildfire smoke particles into the moist air from above, i.e, from the main smoke reservoir in the lower stratosphere (Ohneiser et al., 2021).

325   As can be seen in Fig. 5, the lidar is able to detect any cirrus structure from the top of the cirrus (ice-generation cells) at 10.5 km height to the base of the virga. In contrast, the cloud radar reflectivity was useful for further analysis up to heights of 7.5 km, only. The blue dashed line in Fig. 5 marks the height up to which radar reflectivity data are available for the derivation of cirrus microphysical properties. The strong increase of the backscatter signal strength with decreasing height is a clear sign for the increasing size of ice crystals.

330   The microphysical properties derived from the combined lidar and radar observations by means of our LIRAS-ice scheme (Sect 2.5) are shown in Fig. 7. The top panel shows the Z/E data field that serves as measured input in the retrieval. The derived IWC mostly shows values from 0.0001 to 0.01 g m^{-3} which is typical for thin cirrus. The IWC signatures are well correlated with the virga structures. The majority of the derived ICNC values were in the range from 0.1-10 L^{-1}. Even if we consider the large uncertainty in the retrieved ICNC of a factor of 3 and that aggregation of crystals during falling may have 335 reduced the ICNC numbers by a factor of 5-10 in the lower parts of the virga (Field et al., 2006), the estimated ICNC values point to heterogeneous ice nucleation as the dominant ice-nucleation mode.

     Figure 8 compiles cirrus geometrical and optical properties, meteorological conditions, cirrus relevant smoke properties, and ICNC numbers in the virga height range from which one may conclude that ICNC in the ice-nucleation zone around 10.5 km
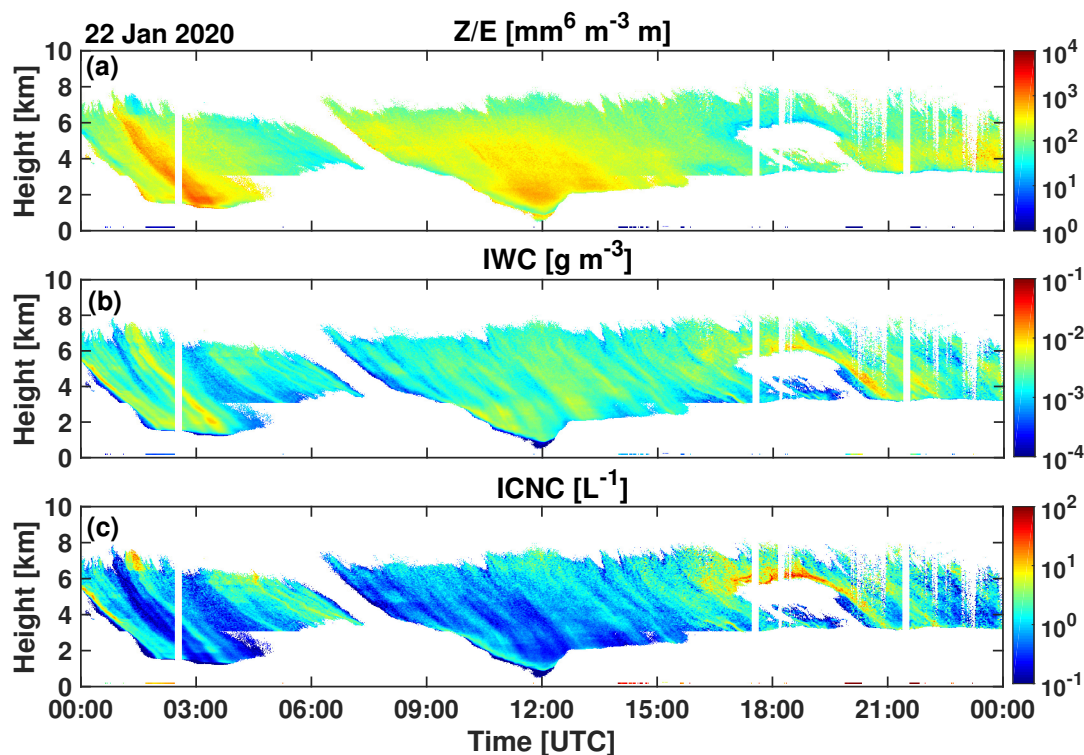
Figure 7. (a) Ratio Z/E with radar reflectivity Z and 532 nm cirrus extinction coefficient E observed on 22 January 2020, (b) LIRAS-ice retrieval of ice water content IWC, and (c) LIRAS-ice retrieval of ice crystal number concentration ICNC.

height was probably not very different from the virga ICNC values around 1 L^{-1}. Panel a shows mean height profiles (1-
340   2.5 hour mean profiles) of the cirrus extinction coefficient indicating the cirrus height range from top to bottom. Three different
periods of cirrus evolution on 22 January (2-14 UTC) are selected. Panel b indicates rather stable meteorological conditions
in terms of temperature and relative humidity over ice RH$_i$ as measured with radiosondes launched at 23 UTC on 21 January,
and at 5, 11, and 17 UTC on 22 January. The ice saturation ratio varied around 1.0 (equilibrium conditions) in the more than
8 km deep virga and showed values up to 1.2-1.35 at the top of the cirrus system (in the ice nucleation zone). Panel c shows
345   profiles of the particle surface area concentration (PSAC) of the smoke particles as estimated from lidar observations during
clear-sky conditions in the morning of 21 January 2020 and after the long-lasting 5-day cirrus event on 27 January 2020. The
PSAC maximum was found around and just above the tropopause during the winter months from November 2019 to March
2020 (Ohneiser et al., 2021) with values close to 10 μm^2 cm^{-3}. Panel d finally presents mean ICNC profiles (mean values for
approximately 1 hour) for the virga height range from 7.5 km down to about 1.5 km height. The retrieved low ICNC values
350   around 1 L^{-1} clearly indicate the dominance of heterogeneous ice nucleation.

The PSAC profiles in Fig. 8c, observed before and after the period with strong cirrus formation from 21-26 January 2020
(further discussed in part 2), do not indicate any decrease in the PSAC values. This finding may be used as an indication
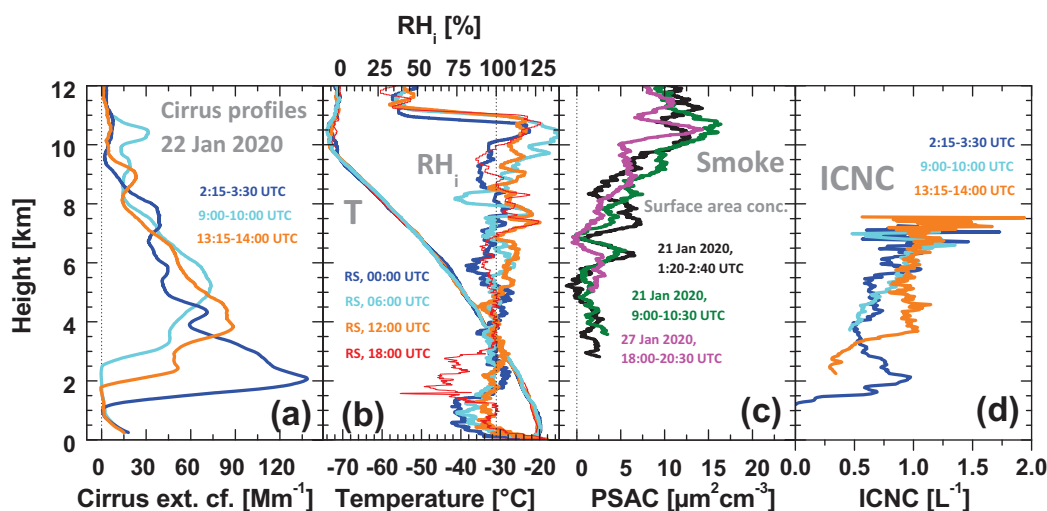
Figure 8. Synergistic overview of (a) cirrus geometrical and optical properties, (b) meteorological conditions in terms of temperature T and relative humidity over ice RH_i measured with 4 radiosondes (RS), (c) aerosol pollution levels, and (d) ice crystal number concentrations (ICNC) in the ice virga, obtained from combined lidar-radar observations.

that the INP reservoir was much larger than the number concentration of the INPs involved in the ice nucleation processes, as suggested by Knopf et al. (2023). In other words, the INP reservoir was not depleted by ice crystal formation. The lidar

355   conversions indicated n_{250} values of 2000 L^{-1}, the observed virga ICNC values in panel d are of the order of 1 L^{-1}, and are probably not larger than 10 L^{-1} in the cirrus generation cells.

3.4   Combined lidar-radar observations: 20 independent cirrus cases

Figure 9 shows further ICNC height time displays for cirrus events on 23 November 2019, 6 December 2019, and 24 January 2020. The 6 December lidar measurement was already presented and discussed in Engelmann et al. (2021). Again, in the lower

360   part of the virga the dark blue colors (ICNC<1 L^{-1}) dominate. ICNC values of 10-50 L^{-1} were partly obtained at the top of the colored virga fields (yellow to orange colors). The cirrus nucleation zone was at 9 km height on 23 November (cirrus top temperature of $-64°C$, RH_i of 143%), around 9-9.5 km on 6 December 2019 (cirrus top temperature of $-63°C$, RH_i of 131%) and at about 10 km on 24 January 2020 (cirrus top temperature of $-72°C$, RH_i of 133%). Large fractions of the virga show dark blue to cyan colors and thus ICNC of the order of 0.01-10 L^{-1}.

365   On 23 November 2019, favorable calm and almost windless conditions were given with wind speeds of 0-3 m s^{-1} in the lowermost 400 m of the atmosphere according to the radiosondes launched at 5 and 11 UTC. The cirrus virga reached the ground (Fig. 9a) so that the 2DVD aboard Polarstern could measure the incoming ice crystal flux. We used this lucky opportunity for comparison of the disdrometer output (ice crystal number concentration, size and shape information) with the lidar-radar-derived ICNC profiles. The comparison is shown in Fig. 10. The ice saturation ratio was >1.0 down to the ground
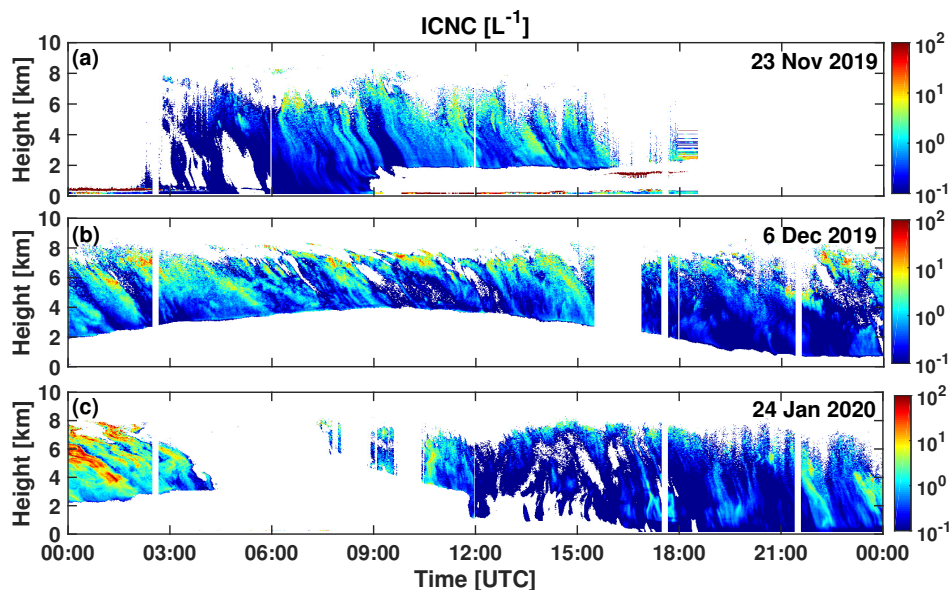
Figure 9. ICNC height time displays obtained by means of the LIRAS-ice retrieval scheme in the virga zones for (a) 23 November 2019 (at 85.7°N, 120°E), (b) 6 December 2019 (at 86.1°N, 122°E), and (c) 24 January 2020 (at 87.4°N, 93°E). Cirrus top height was at about 9 km on 23 November (a) and 6 December (b), and 10 km on 24 January (c). The Polarstern drifted with the pack ice slowly towards the west in December and January (see Fig. 1).

370   (see Fig. 10) so that sublimation of ice crystals during falling did not occur. The temperatures in all cases were below -20°C. Strong variability was visible in the highly resolved ICNC time series recorded with the 2DVD. Therefore, we compare 1 hour mean disdrometer values with 2 hour mean ICNC profiles.

    The agreement in Fig. 10 is reasonably good when keeping an uncertainty of a factor 3 in the LIRAS-ice products into consideration. Both approaches show low ICNC values <1 L^{-1}. The lowest remote sensing height bin is 250 m above Po-
375 larstern. The decrease of ICNC with increasing falling distance may indicate the impact of continuously occurring collision and aggregation events during falling over many hours. The 2DVD observations also indicated crystal diameters clearly larger than 150 micrometer, most crystals showed sizes around 500 μm, and bullet-rosette-like crystals shapes. The question arises how crystal collision and aggregation processes are possible if the ICNC values are so low. The ice crystals are formed at different times, and thus grew over different time periods in a given air parcel and thus may cover a large size and falling
380 velocity spectrum. This effect favors collisions. On the other hand, ice growth rates are still not well known as a function of temperature, crystal shape, and crystal size (Kärcher et al., 2023). There many open questions concerning the evolution of the ice crystal characteristics during the life time of a cirrus cloud system.

    Figure. 11 shows 20 profiles (from lidar and radar observations averaged over 1-2 hours) of ICNC, IWC and cirrus extinction coefficients. These 20 observations were performed in 12 different cirrus systems (1 in November, 2 in December, 5 in January,
385 and 4 in February). The data of these 20 profiles provide a realistic picture of the range of MOSAiC winter cirrus IWC and
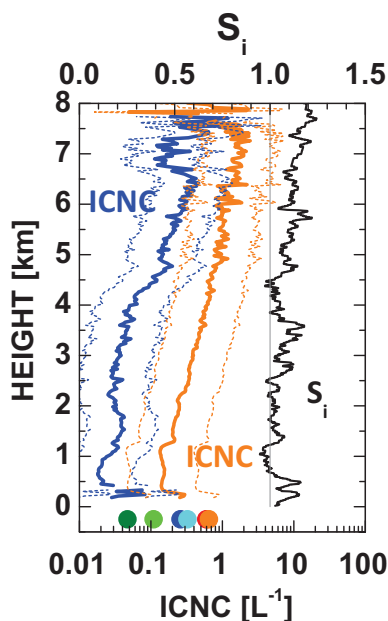
Figure 10. Comparison of hourly mean values of ICNC measured with 2DVD aboard Polarstern (circles at the bottom of the panel, blue: 3-4 UTC, cyan: 4-5 UTC, olive 5-6 UTC, green: 6-7 UTC, red: 7-8 UTC, orange: 8-9 UTC) with ICNC profiles retrieved from the lidar-radar observations (2 hour mean profiles, 3-5 UTC in blue, 7-9 UTC in orange). The dashed curves show the uncertainty margin (mean profile multiplied and divided by 3). The ice saturation ratio S_i measured with radiosonde launched at 5 UTC is shown in black. The S_i profile indicates that evaporation of ice crystals did not occur over the entire sedimentation height range.

ICNC values in the virga below cirrus nucleation cells. The ICNC values were mostly in the range from 0.01-1 L^{-1}, IWC showed typically values from 0.001 to 0.02 g m^{-3}, and the extinction values were mostly between 30 and 300 Mm^{-1}.

Heymsfield et al. (2014) presented correlations between the ice extinction coefficient, calculated from in situ measured ice crystal size spectra, and measured IWC. For the temperature range from -60°C to -20°C (typical temperatures in the MOSAiC cirrus virga zones) the authors found that extinction coefficients of 100 Mm^{-1} correspond to IWC values of about 0.005 g m^{-3}. We found IWCs around 0.0035 g m^{-3} for extinction coefficients around 100 Mm^{-1}. This specific relationship points to large crystals with diameters >100 μm.

Our Arctic cirrus observations are in good agreement with balloon-borne observations of Wolf et al. (2018) at high northern latitudes. The balloons were launched at Kiruna, Sweden, at 68°N. Eight Arctic cirrus profiles were measured in different years (2012-2016), mostly during winter months. On 12 February 2016, a very similar cirrus event as shown in Fig. 5 was observed over the Kiruna region. The ice saturation ratio ranged from 1.0-1.2 in the virga zone, extending from 10 km down to 3.5 km height. The ICNC values ranged from about 3-8 L^{-1} in the virga zone as well as in the cirrus top region. Most of the eight cirrus profiles showed ICNC values of the order of 10-20 L^{-1} (up to 50 L^{-1}) in the ice nucleation regions. ICNC of 100-400 L^{-1} in the cirrus top region was found in two of the eight balloon flights.
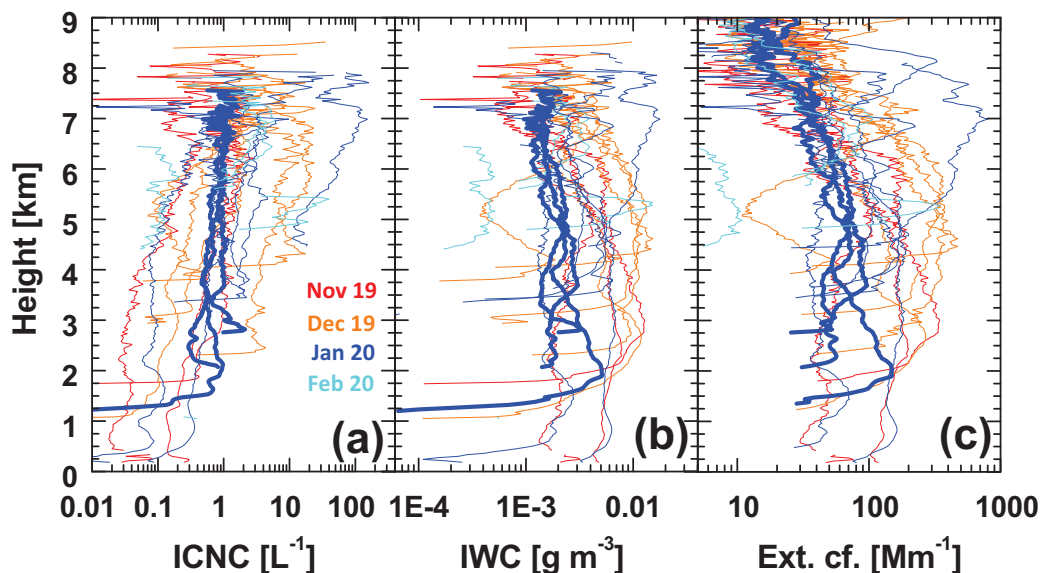
Figure 11. Height profiles of (a) ice crystal number concentration ICNC, (b) ice water content IWC, and (c) cirrus extinction coefficient (532 nm). 20 cirrus profiles are shown (mean profiles average over 1-2 hours). November 2019 profiles are given in red, December 2019 profiles in orange, January 2020 profiles in blue, and February 2020 profiles in cyan. The 3 profiles measured on 22 January (see Fig. 8) are shown in thick blue.

400 Rather similar results as shown in Fig. 11 were obtained during an airborne field campaign at high northern latitudes (60°-76°N, between Scandinavia and Greenland) in June and July 2021 (De La Torre Castro et al., 2023). The airborne in situ observations revealed median values of 1 L^{-1} (0.01-9 L^{-1}, 25th to 75th percentile) for ICNC, 0.0019 g m^{-3} (0.0002 to 0.011 g m^{-3}, 25th to 75th percentile) for IWC, and 210 μm (146-320 μm, 25th to 75th percentile) regarding crystal size. Cirrus extinction coefficients accumulated between 1 and 500 Mm^{-1}.

405 The final figure in this part 1 is given as an introduction to part 2. The specific cirrus humidity and upper tropospheric aerosol conditions during the MOSAiC winter half year pointing to a significant impact of wildfire smoke particles on ice nucleation are shown in Fig. 12. The maximum ice supersaturation ratio, found in 30 cirrus radiosonde profiles (measured during the 20 cirrus events considered in Fig. 11) is shown. 20 of the 30 values were larger than 1.3 in the presence of high smoke pollution levels characterized by PSAC values around 10 μm^2 cm^{-3}. All clear sky lidar observations performed in the four months from
410 November 2019 to February 2020 are shown. The high supersaturation values indicate relatively poor INPs. In the case of good INPs, such as dust INPs, ice supersaturation values would probably be below 1.3 (Ullrich et al., 2017; Ansmann et al., 2019; Dekoutsidis et al., 2024). In part 2, we will continue our Arctic cirrus studies and present the key finding of MOSAiC-related simulation studies.
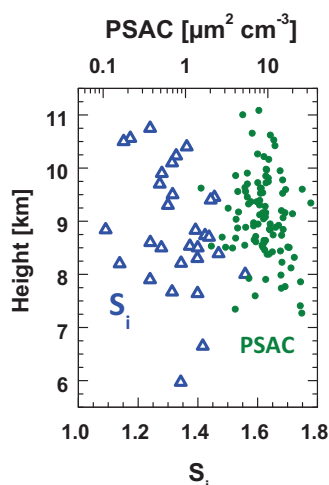
Figure 12. Maximum (peak) cirrus ice supersaturation ratio $S_{i,max}(z)$ observed at height z with radiosonde during the ascent through 30 cirrus layers (open blue triangles). In addition, particle surface are concentrations (PSAC) for the tropopause region, obtained from clear sky lidar observations (November 2019 to February 2020) are shown (green circles).

4   Summary

415   For the first time, an Arctic cirrus data set was presented that covers geometrical, optical, and microphyscial properties of ice clouds measured at latitudes >85°N during the winter half year from October 2019 to March 2020. The investigation was based on modern remote sensing analysis methods. Respective lidar and cloud radar observations were performed aboard the German ice breaker Polarstern as part of the MOSAiC expedition, the largest Arctic field campaign ever conducted. All detected and analyzed cirrus fields belong to the synoptic cirrus category (characterized by a top-down generation of the cirrus structures).

420   The ice clouds were mostly optically thin with cloud mean 532 nm extinction coefficients ranging from about 30-300 Mm^{-1} in most cases, with IWC and ICNC values mostly frequently between 0.001 and 0.02 g m^{-3} and 0.01-10 L^{-1}, respectively.

Goal of the data analysis in this part 1 was to provide observational evidence for a dominating impact of aged wildfire smoke (organic aerosol particles) on cirrus formation in the central Arctic (over the MOSAiC research icebreaker Polarstern) during the winter half year of 2019-2020. As a result, the combination of (a) low ICNC of typically 0.1-10 L in ice virga, pointing

425   to the dominance of heterogeneous ice nucleation, (b) observed high ice saturation ratios accumulating at 1.3-1.4 in the upper part of the cirrus clouds, and (c) the occurrence of significantly elevated levels of smoke aerosol pollution characterized by particle surface area concentrations of 5–15 μm^2 cm^{-3} corroborate our hypothesis that wildfire smoke particles, expected to be inefficient INPs compared to efficient dust INPs, were responsible for many of the observed Arctic cirrus systems showing low ICNCs.

430   Not only the ice clouds but also the aerosol conditions (here wildfire smoke pollution) were quantified in terms of particle surface area and number concentration so that an investigation of the impact of the wildfire smoke on ice formation with the

help of simulations can be based on realistic (measured) aerosol conditions in part 2 (Ansmann et al., 2024a). Modeling allows us to characterize the role af aerosol particles, serving as ice nucleating particles) in the context of the given meteorological conditions (temperature, relative humidity, vertical velocities at cirrus top) in heterogeneous ice formation processes. In part 2,
435 the main findings of the entire study are discussed and conclusions on the impact of smoke on cirrus formation are drawn.

Aim of the simulations in part 2 is to gain a deeper and more detailed insight into the potential smoke impact on ice nucleation as a function of observed aerosol and meteorological conditions (temperature, relative humidity) and by considering realistic gravity wave characteristics (updraft speed, wave amplitude). Vertical movements of air parcels are essential to initiate cloud formation.

5 Data availability

Polly lidar observations (level 0 data, measured signals) are in the PollyNet database (**?**). All the analysis products are available at TROPOS upon request (polly@tropos.de) and at https://doi.pangaea.de/10.1594/PANGAEA.935539 (Ohneiser et al., 2021). Cloud radar data are downloaded from the ARM data base (ARM, 2024; ARM-MOSAiC, 2024). MOSAiC radiosonde data are available at https://doi.org/10.1594/PANGAEA.928656 (Maturilli et al., 2021, 2022) Backward trajectory analysis has been
445 performed by air mass transport computation with the NOAA (National Oceanic and Atmospheric Administration) HYSPLIT (HYbrid Single-Particle Lagrangian Integrated Trajectory) model (HYSPLIT, 2024). LIRAS-ice products can be obtained on request (by contacting the corresponding author)

6 Author contributions

The paper was written and designed by AA and CJ. The aerosol and cloud data analysis was performed by CJ, JR, JB, KO,
450 HG, JH, DA, TG, and PS. RE, HGr, MR, JH, and DA took care of the lidar observations aboard Polarstern during the one year MOSAiC expedition. SD was responsible for the data analysis of the Polarstern radiosonde observations and related quality assurance efforts. DAK and UW were involved in the interpretation of the findings. All coauthors were actively involved in the extended discussions and the elaboration of the final design of the manuscript.

7 Competing interests

455 Daniel A. Knopf is a member of the editorial board of Atmospheric Chemistry and Physics

8 Financial support

The Multidisciplinary drifting Observatory for the Study of the Arctic Climate (MOSAiC) program was funded by the German Federal Ministry for Education and Research (BMBF) through financing the Alfred Wegener Institut Helmholtz Zentrum für

Polar und Meeresforschung (AWI) and the Polarstern expedition PS122 under grant N-2014-H-060_Dethloff. The lidar analy-
sis on smoke-cirrus interaction was further supported by BMBF funding of the SCiAMO project (MOSAIC-FKZ 03F0915A).
The radiosonde program was funded by AWI awards AFMOSAiC-1_00 and AWI_PS122_00, the U.S. Department of Energy
Atmospheric Radiation Measurement Program, and the German Weather Service. This project has also received funding from
the European Union's Horizon 2020 research and innovation program ACTRIS-2 Integrating Activities (H2020-INFRAIA-
2014 - 2015, grant agreement no. 654109). We gratefully acknowledge the funding by the Deutsche Forschungsgemeinschaft
(DFG, German Research Foundation) – project no. 268020496 - TRR 172, within the Transregional Collaborative Research
Center "ArctiC Amplification: Climate Relevant Atmospheric and SurfaCe Processes, and Feedback Mechanisms (AC)3".
DAK acknowledges support by U.S. Department of Energy's (DOE) Atmospheric System Research (ASR) program, Office of
Biological and Environmental Research (OBER) (grant no. DE-SC0021034).

Acknowledgements. Data used in this article were produced as part of the international Multidisciplinary drifting Observatory for the Study
of the Arctic Climate (MOSAiC) with the tag MOSAiC20192020 and the Project_ID: AWI_PS122_00. We would like to thank everyone
who contributed to the measurements used here (Nixdorf et al., 2021). Radiosonde data were obtained through a partnership between the
leading Alfred Wegener Institute, the Atmospheric Radiation Measurement user facility, a U.S. Department of Energy facility managed by
the Biological and Environmental Research Program, and the German Weather Service (DWD). We would like to thank the RV Polarstern
crew for their perfect logistical support during the one-year MOSAiC expedition.

References

475 **References**

Abatzoglou, J. T., Williams, A. P., and Barbero, R.: Global emergence of anthropogenic climate change in fire weather indices, Geophys, Res. Lett., 46, 326–336, https://doi.org/10.1029/2018GL080959, 2019.

Alpert, P. A., Aller, J. Y., and Knopf, D. A.: Initiation of the ice phase by marine biogenic surfaces in supersaturated gas and supercooled aqueous phases, Phys. Chem. Chem. Phys., 13, 19 882–19 894, https://doi.org/10.1039/C1CP21844A, 2011.

480 Ansmann, A., Wandinger, U., Riebesell, M. A., Weitkamp, C., and Michaelis, W.: Independent measurement of extinction and backscatter profiles in cirrus clouds by using a combined Raman elastic-backscatter lidar, Appl. Opt., 31, 7113–7131, https://doi.org/10.1364/AO.31.007113, 1992.

Ansmann, A., Mamouri, R.-E., Bühl, J., Seifert, P., Engelmann, R., Hofer, J., Nisantzi, A., Atkinson, J. D., Kanji, Z. A., Sierau, B., Vrekoussis, M., and Sciare, J.: Ice-nucleating particle versus ice crystal number concentration in altocumulus and cirrus layers embedded in
485 Saharan dust: a closure study, Atmospheric Chemistry and Physics, 19, 15 087–15 115, https://doi.org/10.5194/acp-19-15087-2019, 2019.

Ansmann, A., Ohneiser, K., Mamouri, R.-E., Knopf, D. A., Veselovskii, I., Baars, H., Engelmann, R., Foth, A., Jimenez, C., Seifert, P., and Barja, B.: Tropospheric and stratospheric wildfire smoke profiling with lidar: mass, surface area, CCN, and INP retrieval, Atmospheric Chemistry and Physics, 21, https://doi.org/10.5194/acp-21-9779-2021, 2021.

Ansmann, A., Ohneiser, K., Chudnovsky, A., Knopf, D. A., Eloranta, E. W., Villanueva, D., Seifert, P., Radenz, M., Barja, B.,
490 Zamorano, F., Jimenez, C., Engelmann, R., Baars, H., Griesche, H., Hofer, J., Althausen, D., and Wandinger, U.: Ozone depletion in the Arctic and Antarctic stratosphere induced by wildfire smoke, Atmospheric Chemistry and Physics Discussions, 2022, 1–42, https://doi.org/10.5194/acp-2022-247, 2022.

Ansmann, A., Ohneiser, K., Engelmann, R., Radenz, M., Griesche, H., Hofer, J., Althausen, D., Creamean, J. M., Boyer, M. C., Knopf, D. A., Dahlke, S., Maturilli, M., Gebauer, H., Bühl, J., Jimenez, C., Seifert, P., and Wandinger, U.: Annual cycle of aerosol properties
495 over the central Arctic during MOSAiC 2019–2020 – light-extinction, CCN, and INP levels from the boundary layer to the tropopause, Atmospheric Chemistry and Physics, 23, 12 821–12 849, https://doi.org/10.5194/acp-23-12821-2023, 2023.

Ansmann, A., Jimenez, C., Knopf, D. A., Roschke, J., Bühl, J., Ohneiser, K., and Engelmann, R.: Impact of wildfire smoke on Arctic cirrus formation, part 2: simulation of MOSAiC 2019-2020 cases, EGUsphere, 2024, 1–YYY, https://doi.org/10.5194/egusphere-2024-XXXX, 2024a.

500 Ansmann, A., Veselovskii, I., Ohneiser, K., and Chudnovsky, A.: Comment on "Stratospheric Aerosol Composition Observed by the Atmospheric Chemistry Experiment Following the 2019 Raikoke Eruption" by Boone et al., Journal of Geophysical Research: Atmospheres, 129, e2022JD038 080, https://doi.org/10.1029/2022JD038080, e2022JD038080 2022JD038080, 2024b.

ARM-MOSAiC(2024): Atmospheric Radiation Measurement (ARM) user facility, 2019, updated hourly, Ka ARM Zenith Radar (KAZR-CFRGE), 2019-10-11 to 2020-09-20, ARM Mobile Facility (MOS) MOSAIC (Drifting Obs - Study of Arctic Climate), AMF2 (M1),
505 compiled by I. Lindenmaier, D. Nelson, B. Isom, J. Hardin, A. Matthews, T. Wendler, and V. Castro, ARM Data Center, last access: 13 February, 2024.

ARM(2024): Atmospheric Radiation Measurement (ARM) user facility, data are collected through routine operations and scientific field experiments, US Department of Energy (DOE), available at https://arm.gov/data, last access: 22 January 2024, 2024.

Baars, H., Kanitz, T., Engelmann, R., Althausen, D., Heese, B., Komppula, M., Preißler, J., Tesche, M., Ansmann, A., Wandinger, U., Lim,
510 J.-H., Ahn, J. Y., Stachlewska, I. S., Amiridis, V., Marinou, E., Seifert, P., Hofer, J., Skupin, A., Schneider, F., Bohlmann, S., Foth, A., Bley, S., Pfüller, A., Giannakaki, E., Lihavainen, H., Viisanen, Y., Hooda, R. K., Pereira, S. N., Bortoli, D., Wagner, F., Mattis, I., Janicka,

L., Markowicz, K. M., Achtert, P., Artaxo, P., Pauliquevis, T., Souza, R. A. F., Sharma, V. P., van Zyl, P. G., Beukes, J. P., Sun, J., Rohwer, E. G., Deng, R., Mamouri, R.-E., and Zamorano, F.: An overview of the first decade of Polly[NET]: an emerging network of automated Raman-polarization lidars for

515   continuous aerosol profiling, Atmospheric Chemistry and Physics, 16, 5111–5137, https://doi.org/10.5194/acp-16-5111-2016, 2016.

Baars, H., Ansmann, A., Ohneiser, K., Haarig, M., Engelmann, R., Althausen, D., Hanssen, I., Gausa, M., Pietruczuk, A., Szkop, A., Stach-lewska, I. S., Wang, D., Reichardt, J., Skupin, A., Mattis, I., Trickl, T., Vogelmann, H., Navas-Guzmán, F., Haefele, A., Acheson, K., Ruth, A. A., Tatarov, B., Müller, D., Hu, Q., Podvin, T., Goloub, P., Veselovskii, I., Pietras, C., Haeffelin, M., Fréville, P., Sicard, M., Comerón, A., Fernández García, A. J., Molero Menéndez, F., Córdoba-Jabonero, C., Guerrero-Rascado, J. L., Alados-Arboledas, L., Bortoli, D.,

520   Costa, M. J., Dionisi, D., Liberti, G. L., Wang, X., Sannino, A., Papagiannopoulos, N., Boselli, A., Mona, L., D'Amico, G., Romano, S., Perrone, M. R., Belegante, L., Nicolae, D., Grigorov, I., Gialitaki, A., Amiridis, V., Soupiona, O., Papayannis, A., Mamouri, R.-E., Nisantzi, A., Heese, B., Hofer, J., Schechner, Y. Y., Wandinger, U., and Pappalardo, G.: The unprecedented 2017–2018 stratospheric smoke event: decay phase and aerosol properties observed with the EARLINET, Atmospheric Chemistry and Physics, 19, 15 183–15 198, https://doi.org/10.5194/acp-19-15183-2019, 2019.

525   Bailey, M. and Hallett, J.: Growth Rates and Habits of Ice Crystals between -20° and -70°C, Journal of the Atmospheric Sciences, 61, 514 – 544, https://doi.org/10.1175/1520-0469(2004)061<0514:GRAHOI>2.0.CO;2, 2004.

Bailey, M. and Hallett, J.: Ice Crystal Linear Growth Rates from -20° to -70°C: Confirmation from Wave Cloud Studies, Journal of the Atmospheric Sciences, 69, 390 – 402, https://doi.org/10.1175/JAS-D-11-035.1, 2012.

Bühl, J., Seifert, P., Radenz, M., Baars, H., and Ansmann, A.: Ice crystal number concentration from lidar, cloud radar and radar wind profiler

530   measurements, Atmospheric Measurement Techniques, 12, 6601–6617, https://doi.org/10.5194/amt-12-6601-2019, 2019.

De La Torre Castro, E., Jurkat-Witschas, T., Afchine, A., Grewe, V., Hahn, V., Kirschler, S., Krämer, M., Lucke, J., Spelten, N., Wernli, H., Zöger, M., and Voigt, C.: Differences in microphysical properties of cirrus at high and mid-latitudes, Atmospheric Chemistry and Physics, 23, 13 167–13 189, https://doi.org/10.5194/acp-23-13167-2023, 2023.

Dekoutsidis, G., Wirth, M., and Groß, S.: The effects of warm-air intrusions in the high Arctic on cirrus clouds, Atmospheric Chemistry and

535   Physics, 24, 5971–5987, https://doi.org/10.5194/acp-24-5971-2024, 2024.

DeMott, P. J., Prenni, A. J., Liu, X., Kreidenweis, S. M., Petters, M. D., Twohy, C. H., Richardson, M. S., Eidhammer, T., and Rogers, D. C.: Predicting global atmospheric ice nuclei distributions and their impacts on climate, Proc. Natl. Acad. Sci. USA, 107, 11 217–11 222, https://doi.org/10.1073/pnas.0910818107, 2010.

Engelmann, R., Kanitz, T., Baars, H., Heese, B., Althausen, D., Skupin, A., Wandinger, U., Komppula, M., Stachlewska, I. S., Amiridis, V.,

540   Marinou, E., Mattis, I., Linné, H., and Ansmann, A.: The automated multiwavelength Raman polarization and water-vapor lidar Polly[XT]: the neXT generation, Atmospheric Measurement Techniques, 9, 1767–1784, https://doi.org/10.5194/amt-9-1767-2016, 2016.

Engelmann, R., Ansmann, A., Ohneiser, K., Griesche, H., Radenz, M., Hofer, J., Althausen, D., Dahlke, S., Maturilli, M., Veselovskii, I., Jimenez, C., Wiesen, R., Baars, H., Bühl, J., Gebauer, H., Haarig, M., Seifert, P., Wandinger, U., and Macke, A.: Wildfire smoke, Arctic haze, and aerosol effects on mixed-phase and cirrus clouds over the North Pole region during MOSAiC: an introduction, Atmospheric

545   Chemistry and Physics, 21, https://doi.org/10.5194/acp-21-13397-2021, 2021.

Fetterer, F., Knowles, K., Meier, W. N., Savoie, M., and Windnagel, A. K.: Sea Ice Index, Version 3, Monthly Sea Ice Extent. Boulder, Colorado USA. NSIDC: National Snow and Ice Data Center, https://doi.org/10.7265/N5K072F8, 2017.

Field, P. R., Heymsfield, A. J., and Bansemer, A.: A Test of Ice Self-Collection Kernels Using Aircraft Data, Journal of the Atmospheric Sciences, 63, 651 – 666, https://doi.org/10.1175/JAS3653.1, 2006.

550 Garnier, A., Pelon, J., Vaughan, M. A., Winker, D. M., Trepte, C. R., and Dubuisson, P.: Lidar multiple scattering factors inferred from CALIPSO lidar and IIR retrievals of semi-transparent cirrus cloud optical depths over oceans, Atmospheric Measurement Techniques, 8, 2759–2774, https://doi.org/10.5194/amt-8-2759-2015, 2015.

Gaudek, T.: Co-located observations of liquid and ice precipitation hydrometeors with a two-dimensional video disdrometer, a holographic cloud in-situ sonde, and active remote sensing, Master Thesis, Leipzig University, p. 65 pages, 2024.

555 Giannakaki, E., Balis, D. S., Amiridis, V., and Kazadzis, S.: Optical and geometrical characteristics of cirrus clouds over a Southern European lidar station, Atmospheric Chemistry and Physics, 7, 5519–5530, https://doi.org/10.5194/acp-7-5519-2007, 2007.

Haarig, M., Engelmann, R., Ansmann, A., Veselovskii, I, Whiteman, D. N., and Althausen, D.: 1064 nm rotational Raman lidar for particle extinction and lidar-ratio profiling: cirrus case study, Atmospheric Measurement Techniques, 9, 4269–4278, https://doi.org/10.5194/amt-9-4269-2016, 2016.

560 Heymsfield, A., Winker, D., Avery, M., Vaughan, M., Diskin, G., Deng, M., Mitev, V., and Matthey, R.: Relationships between Ice Water Content and Volume Extinction Coefficient from In Situ Observations for Temperatures from 0° to -86°C: Implications for Spaceborne Lidar Retrievals, Journal of Applied Meteorology and Climatology, 53, 479 – 505, https://doi.org/10.1175/JAMC-D-13-087.1, 2014.

Heymsfield, A. J., Krämer, M., Luebke, A., Brown, P., Cziczo, D. J., Franklin, C., Lawson, P., Lohmann, U., McFarquhar, G., Ulanowski, Z., and Tricht, K. V.: Cirrus Clouds, Meteorological Monographs, 58, 2.1 – 2.26, https://doi.org/10.1175/AMSMONOGRAPHS-D-16-0010.1,
565 2017.

Hofer, J., Althausen, D., Abdullaev, S. F., Makhmudov, A. N., Nazarov, B. I., Schettler, G., Engelmann, R., Baars, H., Fomba, K. W., Müller, K., Heinold, B., Kandler, K., and Ansmann, A.: Long-term profiling of mineral dust and pollution aerosol with multiwavelength polarization Raman lidar at the Central Asian site of Dushanbe, Tajikistan: case studies, Atmospheric Chemistry and Physics, 17, 14 559–14 577, https://doi.org/10.5194/acp-17-14559-2017, 2017.

570 Hogan, R. J., Francis, P., Flentje, H., Illingworth, A., Quante, M., , and Pelon, J.: Characteristics of mixed-phase clouds. I: Lidar, radar and aircraft observations from CLARE'98, Q. J. Roy. Meteor. Soc., 129, 2089–2116, https://doi.org/10.1256/rj.01.208, 2003.

HYSPLIT(2024): HYbrid Single-Particle Lagrangian Integrated Trajectory model, backward trajectory calculation tool, available at: http://ready.arl.noaa.gov/HYSPLIT_traj.php, last access: 20 January, 2024.

Jahl, L. G., Brubaker, T. A., Polen, M. J., Jahn, L. G., Cain, K. P., Bowers, B. B., Fahy, W. D., Graves, S., and Sullivan, R. C.: Atmospheric
575 aging enhances the ice nucleation ability of biomass-burning aerosol, Sci. Adv., 7, https://doi.org/10.1126/sciadv.abd3440, 2021.

Jahn, L. G., Polen, M. J., Jahl, L. G., Brubaker, T. A., Somers, J., and Sullivan, R. C.: Biomass combustion produces ice-active minerals in biomass-burning aerosol and bottom ash, Proc. Natl. Acad. Sci. U.S.A., 117, 21 928–21 937, https://doi.org/10.1073/pnas.1922128117, 2020.

Jimenez, C., Ansmann, A., Engelmann, R., Donovan, D., Malinka, A., Seifert, P., Wiesen, R., Radenz, M., Yin, Z., Bühl, J., Schmidt, J., Barja,
580 B., and Wandinger, U.: The dual-field-of-view polarization lidar technique: a new concept in monitoring aerosol effects in liquid-water clouds – case studies, Atmospheric Chemistry and Physics, 20, 15 265–15 284, https://doi.org/10.5194/acp-20-15265-2020, 2020.

Jolly, W. M., Cochrane, M. A., Freeborn, P. H., Holden, Z. A., Brown, T. J., Williamson, G. J., and Bowman, D. M. J. S.: Climate-induced variations in global wildfire danger from 1979 to 2013, Nature Communications, 6, https://doi.org/10.1038/ncomms8537, 2015.

Josset, D., Pelon, J., Garnier, A., Hu, Y., Vaughan, M., Zhai, P.-W., Kuehn, R., and Lucker, P.: Cirrus optical depth and lidar ratio re-
585 trieval from combined CALIPSO-CloudSat observations using ocean surface echo, Journal of Geophysical Research: Atmospheres, 117, https://doi.org/10.1029/2011JD016959, 2012.

Jäger, H.: Long-term record of lidar observations of the stratospheric aerosol layer at Garmisch-Partenkirchen, Journal of Geophysical Research: Atmospheres, 110, https://doi.org/https://doi.org/10.1029/2004JD005506, 2005.

Kanji, Z. A., Florea, O., and Abbatt, J. P. D.: Ice formation via deposition nucleation on mineral dust and organics: dependence of onset relative humidity on total particulate surface area, Environmental Research Letters, 3, 025 004, https://doi.org/10.1088/1748-9326/3/2/025004, 2008.

Kirchmeier-Young, M. C., Gillett, N. P., Zwiers, F. W., Cannon, A. J., and Anslow, F. S.: Attribution of the influence of human- induced climate change on an extreme fire season, Earths Future, 7, 2–10, https://doi.org/10.1029/2018EF001050, 2019.

Knopf, D. A. and Alpert, P. A.: A water activity based model of heterogeneous ice nucleation kinetics for freezing of water and aqueous solution droplets, Farad. Discuss., 165, 513–534, https://doi.org/10.1039/c3fd00035d, 2013.

Knopf, D. A. and Alpert, P. A.: Atmospheric ice nucleation, Nature Reviews Physics, 5, 203–217, https://doi.org/10.1038/s42254-023-00570-7, 2023.

Knopf, D. A., Alpert, P. A., and Wang, B.: The role of organic aerosol in atmospheric ice nucleation: a review, ACS Earth and Space Chemistry, 2, 168–202, https://doi.org/10.1021/acsearthspacechem.7b00120, 2018.

Knopf, D. A., Silber, I., Riemer, N., Fridlind, A. M., and Ackerman, A. S.: A 1D Model for Nucleation of Ice From Aerosol Particles: An Application to a Mixed-Phase Arctic Stratus Cloud Layer, Journal of Advances in Modeling Earth Systems, 15, e2023MS003 663, https://doi.org/10.1029/2023MS003663, e2023MS003663 2023MS003663, 2023.

Knust, R.: Polar Research and Supply Vessel POLARSTERN operated by the Alfred-Wegener-Institute, Journal of large-scale research facilities JLSRF, 3, A119, https://doi.org/10.17815/jlsrf-3-163, 2017.

Koop, T., Luo, B. P., Tsias, A., and Peter, T.: Water activity as the determinant for homogeneous ice nucleation in aqueous solutions, Nature, 406, 611–614, https://doi.org/10.1038/35020537, 2000.

Kruger, A. and Krajewski, W. F.: Two-Dimensional Video Disdrometer: A Description, Journal of Atmospheric and Oceanic Technology, 19, 602 – 617, https://doi.org/10.1175/1520-0426(2002)019<0602:TDVDAD>2.0.CO;2, 2002.

Kärcher, B., DeMott, P. J., Jensen, E. J., and Harrington, J. Y.: Studies on the Competition Between Homogeneous and Heterogeneous Ice Nucleation in Cirrus Formation, Journal of Geophysical Research: Atmospheres, 127, e2021JD035 805, https://doi.org/10.1029/2021JD035805, e2021JD035805 2021JD035805, 2022.

Kärcher, B., Jensen, E. J., Pokrifka, G. F., and Harrington, J. Y.: Ice Supersaturation Variability in Cirrus Clouds: Role of Vertical Wind Speeds and Deposition Coefficients, Journal of Geophysical Research: Atmospheres, 128, e2023JD039 324, https://doi.org/10.1029/2023JD039324, e2023JD039324 2023JD039324, 2023.

Lohmann, U. and Neubauer, D.: The importance of mixed-phase and ice clouds for climate sensitivity in the global aerosol–climate model ECHAM6-HAM2, Atmospheric Chemistry and Physics, 18, 8807–8828, https://doi.org/10.5194/acp-18-8807-2018, 2018.

Lynch, D. K., Sassen, K., Starr, D. O., and Stephens, G.: Cirrus, Oxford University Press, https://doi.org/10.1093/oso/9780195130720.003.0019, 2002.

Mamouri, R.-E., Ansmann, A., Ohneiser, K., Knopf, D. A., Nisantzi, A., Bühl, J., Engelmann, R., Skupin, A., Seifert, P., Baars, H., Ene, D., Wandinger, U., and Hadjimitsis, D.: Wildfire smoke triggers cirrus formation: lidar observations over the eastern Mediterranean, Atmospheric Chemistry and Physics, 23, 14 097–14 114, https://doi.org/10.5194/acp-23-14097-2023, 2023.

Mason, S. L., Hogan, R. J., Bozzo, A., and Pounder, N. L.: A unified synergistic retrieval of clouds, aerosols, and precipitation from EarthCARE: the ACM-CAP product, Atmospheric Measurement Techniques, 16, 3459–3486, https://doi.org/10.5194/amt-16-3459-2023, 2023.

Maturilli, M., Holdridge, D. J., Dahlke, S., Graeser, J., Sommerfeld, A., Jaiser, R., Deckelmann, H., and Schulz, A.: Initial radiosonde data from 2019-10 to 2020-09 during project MOSAiC, https://doi.org/10.1594/PANGAEA.928656, 2021.

Maturilli, M., Sommer, M., Holdridge, D. J., Dahlke, S., Graeser, J., Sommerfeld, A., Jaiser, R., Deckelmann, H., and Schulz, A.: MOSAiC radiosonde data (level 3) [dataset publication series], https://doi.org/10.1594/PANGAEA.943870, 2022.

Murray, B. J., Wilson, T. W., Dobbie, S., and Cui, Z.: Heterogeneous nucleation of ice particles on glassy aerosols under cirrus conditions, Nature Geoscience, 3, 233–237, https://doi.org/10.1038/ngeo817, 2010.

Nakoudi, K., Ritter, C., and Stachlewska, I.: Clouds over the European Arctic (Ny-Ålesund, Svalbard), Remote Sens., 13, 4555, https://doi.org/10.3390/rs13224555, 2021.

Nixdorf, U., Dethloff, K., Rex, M., Shupe, M., Sommerfeld, A., Perovich, D., Nicolaus, M., Heuze´, C., Rabe, B., Loose, B., Damm, E., Gradinger, R., Fong., A, Maslowski, W., Rinke, A., Kwok, R., Spreen, G., Wendisch, M., Herber, A., Hirsekorn, M., Mohaupt, V., Frickenhaus, S., Immerz, A., Weiss-Tuider, K., König, B., Mengedoht, D., Regnery, J., Gerchow, P., Ransby, D., Krumpen, T., Morgenstern, A., Haas, C., Kanzow, T., Rack, F. R., Saitzev, V., Sokolov, V., Makarov, A., Schwarze, S., Wunderlich, T., Wurr, K., and Boetius, A.: MOSAiC extended acknowledgement, Zenodo, https://doi.org/10.5281/zenodo.5179738, 2021.

Ohneiser, K., Ansmann, A., Chudnovsky, A., Engelmann, R., Ritter, C., Veselovskii, I., Baars, H., Gebauer, H., Griesche, H., Radenz, M., Hofer, J., Althausen, D., Dahlke, S., and Maturilli, M.: The unexpected smoke layer in the High Arctic winter stratosphere during MOSAiC 2019–2020, Atmospheric Chemistry and Physics, 21, 15 783–15 808, https://doi.org/10.5194/acp-21-15783-2021, 2021.

Polly(2024): PollyNET lidar data base, available at: http://polly.tropos.de/, last access: 10 January, 2024.

Primm, K., Schill, G., Veghte, D., Freedman, M. A., and Tolbert, M. A.: Depositional ice nucleation on NX illite and mixtures of NX illite with organic acids, J. Atmos. Chem., 74, 55–69, https://doi.org/10.1007/s10874-016-9340-x, 2017.

Pruppacher, H. R. and Klett, J. D.: Microphysics of Clouds and Precipitation, Springer Netherlands, Dordrecht, https://doi.org/10.1007/978-0-306-48100-0, 2010.

Rolph, G., Stein, A., and Stunder, B.: Real-time Environmental Applications and Display sYstem: READY, Environmental Modelling & Software, 95, 210–228, https://doi.org/10.1016/j.envsoft.2017.06.025, 2017.

Sassen, K. and Cho, B. S.: Subvisual-thin cirrus lidar dataset for satellite verification and climatological research, J. Appl. Meteorol., 31, 1275–1285, https://doi.org/10.1175/1520-0450(1992)031<1275:STCLDF>2.0.CO;2, 1992.

Sassen, K., Wang, Z., and Liu, D.: Global distribution of cirrus clouds from CloudSat/Cloud-Aerosol Lidar and Infrared Pathfinder Satellite Observations (CALIPSO) measurements, Journal of Geophysical Research: Atmospheres, 113, https://doi.org/10.1029/2008JD009972, 2008.

Sassen, K., Wang, Z., and Liu, D.: Cirrus clouds and deep convection in the tropics: Insights from CALIPSO and CloudSat, Journal of Geophysical Research: Atmospheres, 114, https://doi.org/10.1029/2009JD011916, 2009.

Schäfer, B., Carlsen, T., Hanssen, I., Gausa, M., and Storelvmo, T.: Observations of cold-cloud properties in the Norwegian Arctic using ground-based and spaceborne lidar, Atmospheric Chemistry and Physics, 22, 9537–9551, https://doi.org/10.5194/acp-22-9537-2022, 2022.

Schröder, F., Kärcher, B., Fiebig, M., and Petzold, A.: Aerosol states in the free troposphere at northern midlatitudes, Journal of Geophysical Research: Atmospheres, 107, LAC 8–1–LAC 8–8, https://doi.org/10.1029/2000JD000194, 2002.

Seifert, P., Ansmann, A., Müller, D., Wandinger, U., Althausen, D., Heymsfield, A. J., Massie, S. T., and Schmitt, C.: Cirrus optical properties observed with lidar, radiosonde, and satellite over the tropical Indian Ocean during the aerosol-polluted northeast and clean maritime southwest monsoon, Journal of Geophysical Research: Atmospheres, 112, https://doi.org/10.1029/2006JD008352, 2007.

Sekelsky, S., Ecklund, W., Firda, J., Gage, K., and R., M.: Particle Size Estimation in Ice-Phase Clouds Using Multifrequency Radar Reflectivity Measurements at 95, 33, and 2.8 GHz, Journal of Applied Meteorology and Climatology, 38, 5–28, https://doi.org/10.1175/1520-0450(1999)038<0005:PSEIIP>2.0.CO;2, 1999.

665 Shupe, M. D., Rex, M., Blomquist, B., Ola, P., Persson, G., Schmale, J., Uttal, T., Althausen, D., Angot, H., Archer, S., Bariteau, L., Beck, I., Bilberry, J., Bucci, S., Buck, C., Boyer, M., Brasseur, Z., Brooks, I. M., Calmer, R., Cassano, J., Castro, V., Chu, D., Costa, D., Cox, C. J., Creamean, J., Crewell, S., Dahlke, S., Damm, E., de Boer, G., Deckelmann, H., Dethloff, K., Dütsch, M., Ebell, K., Ehrlich, A., Ellis, J., Engelmann, R., Fong, A. A., Frey, M. M., Gallagher, M. R., Ganzeveld, L., Gradinger, R., Graeser, J., Greenamyer, V., Griesche, H., Griffiths, S., Hamilton, J., Heinemann, G., Helmig, D., Herber, A., Heuzé, C., Hofer, J., Houchens, T., Howard, D., Inoue, J., Jacobi, H.-

670 W., Jaiser, R., Jokinen, T., Jourdan, O., Jozef, G., King, W., Kirchgaessner, A., Klingebiel, M., Krassovski, M., Krumpen, T., Lampert, A., Landing, W., Laurila, T., Lawrence, D., Lonardi, M., Loose, B., Lüpkes, C., Maahn, M., Macke, A., Maslowski, W., Marsay, C., Maturilli, M., Mech, M., Morris, S., Moser, M., Nicolaus, M., Ortega, P., Osborn, J., Pätzold, F., Perovich, D. K., Petäjä, T., Pilz, C., Pirazzini, R., Posman, K., Powers, H., Pratt, K. A., Preußer, A., Quéléver, L., Radenz, M., Rabe, B., Rinke, A., Sachs, T., Schulz, A., Siebert, H., Silva, T., Solomon, A., Sommerfeld, A., Spreen, G., Stephens, M., Stohl, A., Svensson, G., Uin, J., Viegas, J., Voigt, C., von der Gathen, P.,

675 Wehner, B., Welker, J. M., Wendisch, M., Werner, M., Xie, Z., and Yue, F.: Overview of the MOSAiC expedition: Atmosphere, Elementa: Science of the Anthropocene, 10, https://doi.org/10.1525/elementa.2021.00060, 2022.

Stein, A. F., Draxler, R. R., Rolph, G. D., Stunder, B. J. B., Cohen, M. D., and Ngan, F.: NOAA's HYSPLIT Atmospheric Transport and Dispersion Modeling System, Bulletin of the American Meteorological Society, 96, 2059–2077, https://doi.org/10.1175/BAMS-D-14-00110.1, 2015.

680 Thomas, L., Cartwright, J. C., and Wareing, D. P.: Lidar observations of the horizontal orientation of ice crystals in cirrus clouds, Tellus B, 42, 211–216, https://doi.org/10.1034/j.1600-0889.1990.00001.x-i1, 1990.

Trainer, M. G., Toon, O. B., and Tolbert, M. A.: Measurements of Depositional Ice Nucleation on Insoluble Substrates at Low Temperatures: Implications for Earth and Mars, The Journal of Physical Chemistry C, 113, 2036–2040, https://doi.org/10.1021/jp805140p, 2009.

Trickl, T., Vogelmann, H., Fromm, M. D., Jäger, H., Perfahl, M., and Steinbrecht, W.: Measurement report: Violent biomass burning and

685 volcanic eruptions – a new period of elevated stratospheric aerosol over central Europe (2017 to 2023) in a long series of observations, Atmospheric Chemistry and Physics, 24, 1997–2021, https://doi.org/10.5194/acp-24-1997-2024, 2024.

Ulbrich, C. W.: Natural variations in the analytical form of the raindrop size distribution, J. Climate Appl. Meteor., 22, 1764–1775, https://doi.org/10.1175/1520-0450(1983)022<1764:NVITAF>2.0.CO;2, 1983.

Ullrich, R., Hoose, C., Möhler, O., Niemand, M., Wagner, R., Höhler, K., Hiranuma, N., Saathoff, H., and Leisner, T.: A New Ice Nucleation

690 Active Site Parameterization for Desert Dust and Soot, Journal of the Atmospheric Sciences, 74, 699–717, https://doi.org/10.1175/JAS-D-16-0074.1, 2017.

Vihtakari, M.: ggOceanMaps: Plot data on oceanographic maps using 'ggplot2', https://github.com/MikkoVihtakari/ggOceanMaps, 2020.

Voosen, P.: High-flying wildfire smoke poses potential threat to ozone layer, Science, 374, 921–922, https://doi.org/10.1126/science.acx9655, 2021.

695 Voudouri, K. A., Giannakaki, E., Komppula, M., and Balis, D.: Variability in cirrus cloud properties using a Polly[XT] Raman lidar over high and tropical latitudes, Atmospheric Chemistry and Physics, 20, 4427–4444, https://doi.org/10.5194/acp-20-4427-2020, 2020.

Wang, B. and Knopf, D. A.: Heterogeneous ice nucleation on particles composed of humic-like substances impacted by O_3, Journal of Geophysical Research: Atmospheres, 116, https://doi.org/10.1029/2010JD014964, 2011.

Wang, B., Lambe, A. T., Massoli, P., Onasch, T. B., Davidovits, P., Worsnop, D. R., and Knopf, D. A.: The deposition ice nucleation and
    immersion freezing potential of amorphous secondary organic aerosol: Pathways for ice and mixed-phase cloud formation, Journal of
    Geophysical Research: Atmospheres, 117, https://doi.org/https://doi.org/10.1029/2012JD018063, 2012.

Wolf, V., Kuhn, T., Milz, M., Voelger, P., Krämer, M., and Rolf, C.: Arctic ice clouds over northern Sweden: microphysical prop-
    erties studied with the Balloon-borne Ice Cloud particle Imager B-ICI, Atmospheric Chemistry and Physics, 18, 17 371–17 386,
    https://doi.org/10.5194/acp-18-17371-2018, 2018.

Wolf, V., Kuhn, T., and Krämer, M.: On the Dependence of Cirrus Parametrizations on the Cloud Origin, Geophysical Research Letters, 46,
    12 565–12 571, https://doi.org/10.1029/2019GL083841, 2019.

Xian, P., Zhang, J., O'Neill, N. T., Toth, T. D., Sorenson, B., Colarco, P. R., Kipling, Z., Hyer, E. J., Campbell, J. R., Reid, J. S., and Ranjbar,
    K.: Arctic spring and summertime aerosol optical depth baseline from long-term observations and model reanalyses – Part 1: Climatology
    and trend, Atmospheric Chemistry and Physics, 22, 9915–9947, https://doi.org/10.5194/acp-22-9915-2022, 2022a.

Xian, P., Zhang, J., O'Neill, N. T., Reid, J. S., Toth, T. D., Sorenson, B., Hyer, E. J., Campbell, J. R., and Ranjbar, K.: Arctic spring
    and summertime aerosol optical depth baseline from long-term observations and model reanalyses – Part 2: Statistics of extreme AOD
    events, and implications for the impact of regional biomass burning processes, Atmospheric Chemistry and Physics, 22, 9949–9967,
    https://doi.org/10.5194/acp-22-9949-2022, 2022b.